Structure in the bifurcation diagram of the Duffing oscillator

R. Gilmore and J. W. L. McCallum
Department of Physics and Atmospheric Science, Drexel University, Philadelphia, Pennsylvania 19104
(Received 23 June 1994)

We identify four levels of structure in the bifurcation diagram of the two-well periodically driven Duffing oscillator, plotted as a function of increasing control parameter T, the period of the driving term. The superstructure, or bifurcation peninsula, repeats periodically as T increases by $\sim 2\pi$, beginning and ending with symmetric period-one orbits whose local torsions differ by 2. Within each bifurcation peninsula there is a systematic window structure. The primary window structure is due to Newhouse and Newhouse-like orbits. Fine structure is due to a Farey sequence of well-ordered orbits between the primary windows. Hyperfine structure consists of very narrow windows associated with non-well-ordered orbits. We construct a template for the Duffing oscillator, a two-dimensional return map, and a one-dimensional return map which describes the systematics of orbit creation and annihilation. All structures are identified by topological indices. Our predictions are based on, and compatible with, numerical computations.

PACS number(s): 05.45.+b

I. INTRODUCTION

Extensive numerical simulations of nonlinear oscillators, including the Duffing, Morse, Toda, and bubble oscillators, have revealed striking similarities in their bifurcation diagrams [1–19]. As the period T of the driving force is increased, the bifurcation diagrams of these nonlinear oscillators exhibit almost periodic behavior, with a period approximately equal to the period τ of the unpumped, undamped, linearized oscillator. Each distinct region of the bifurcation diagram between T and $T+\tau$ can be identified by an integer which changes systematically by 1 (2 for Duffing) between adjacent regions [9,12,18,19]. This superstructure [9,12] in the bifurcation diagram is related to the creation and annihilation of period-one orbits by direct and inverse saddle-node bifurcations and the integer which labels this region is the linking number of the period-one orbits [14]. Figure 1 provides a schematic representation of regions in the (λ, T) control parameter space in which many bifurcations take place for a typical nonlinear oscillator. Here λ is the positive Lyapunov exponent. These regions of the

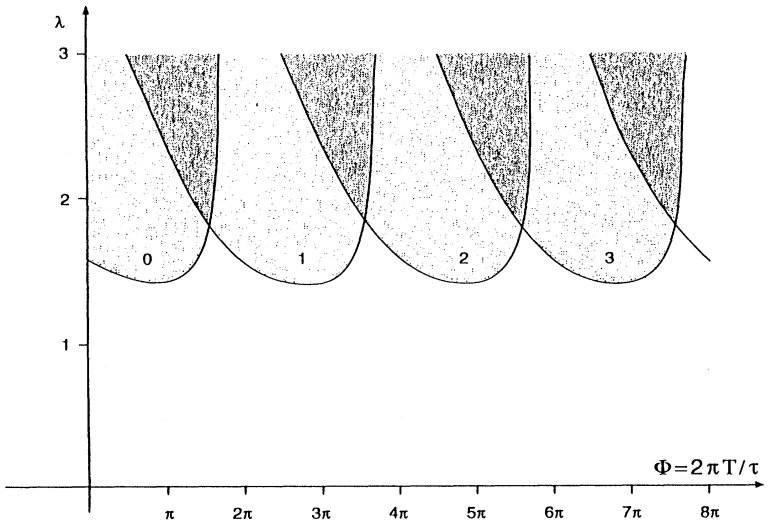

FIG. 1. Schematic representation of the superstructure in the bifurcation diagram of a typical nonlinear oscillator. The regions in which many bifurcations occur are periodic in T, the period of the driving field. For sufficiently small values of λ, the positive Lyapunov exponent, these bifurcation peninsulas are separated by arid oceans in which only period-one orbits exist, while for larger values of the Lyapunov exponent these peninsulas begin to overlap. Successive bifurcation peninsulas are labeled by integers which increase by 1 (2 for the Duffing oscillator) with increasing $\Phi = 2\pi T/\tau$. These peninsulas form the "superstructure" in the bifurcation diagram of nonlinear oscillators. The boundaries of these regions of the superstructure indicate the control parameter values at which the period-three saddle-node bifurcations occur in the one-dimensional return map presented in Eq. (5.4).

superstructure, and the bifurcations which occur in them, are roughly periodic in T.

Within each segment of the bifurcation superstructure of length τ bounded by period-one orbits with local torsion N and $N+1$ ($N+2$ in the Duffing case) there exists a series of windows containing periodic orbits and their associated period-doubling cascades. The window structure is essentially the same within each region of the superstructure. Corresponding windows in different bifurcation regions contain corresponding periodic orbits. The most easily observed windows are associated with Newhouse orbits [20]. Between each pair of windows in this (primary) structure there is fine structure. This consists of narrower windows associated with other well-ordered orbits. There is also a hyperfine structure within each region, consisting of very narrow windows associated with non-well-ordered orbits. In Fig. 2 we show the bifurcation diagram for one of the regions of superstruc-

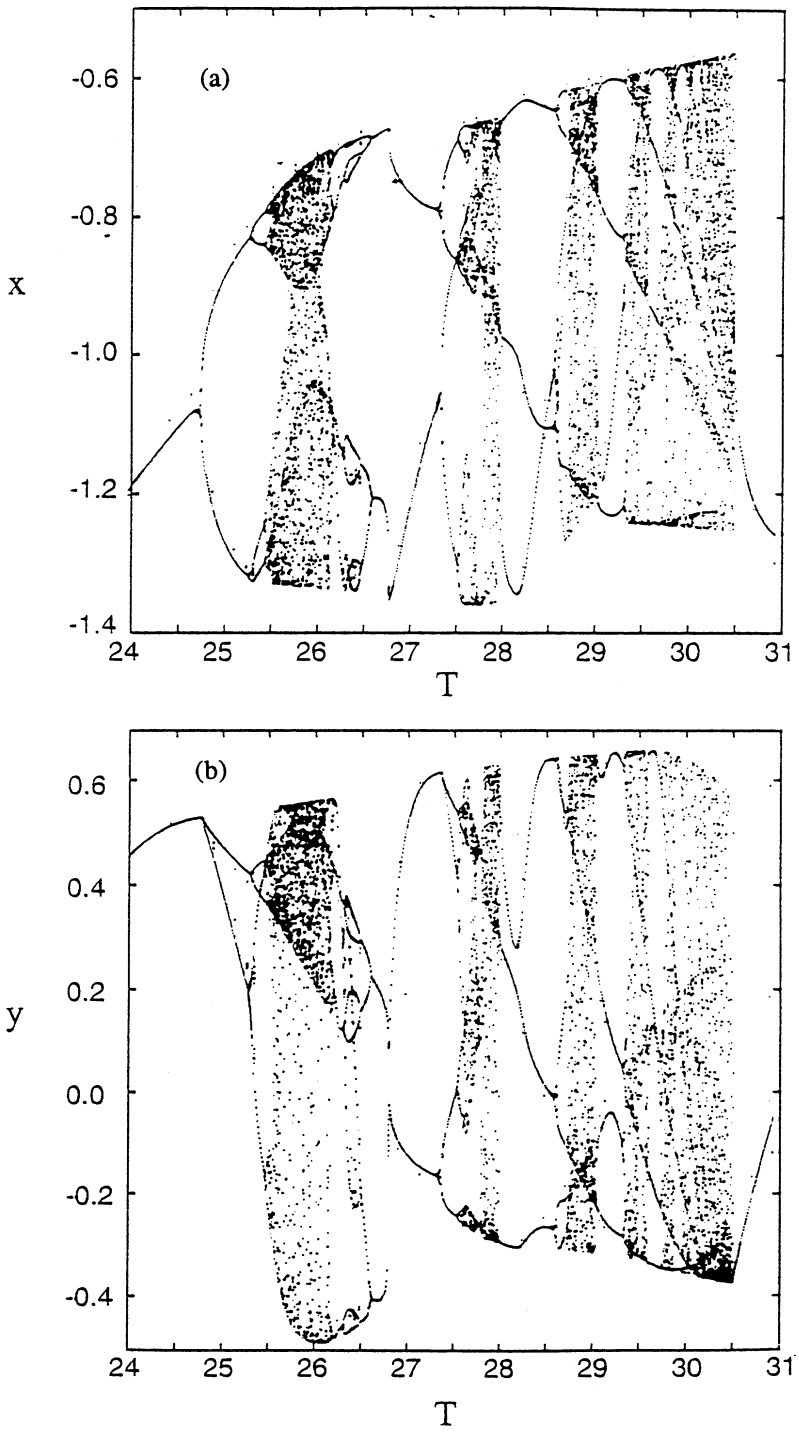

FIG. 2. Bifurcation diagram for the Duffing oscillator (2.3) for $b_0=1.0$, $\delta=\varepsilon/T$, and $\varepsilon=6.0$ in the range $24\le T\le 31$: (a) x vs T and (b) y vs T. The range of the control parameter values lies in the "resonance horn" $R_{6,1}$, using the terminology of Ref. [17]. Within each peninsula the bifurcation diagram shows an alternation between chaotic and periodic behavior. Saddle-node bifurcations create periodic windows. The organization of the periodic windows is essentially the same within each bifurcation peninsula.

ture of the Duffing oscillator [19,21].

In this work we attempt to provide an understanding of the regularities in these bifurcation diagrams and to describe the regular features with a set of topological indices. To do this we construct a template to describe strange attractors which occur in general nonlinear oscillators and the Duffing oscillator. We use these templates [22–25] to account for the systematic variation of the global torsion which identifies each segment of the superstructure. We also use these templates to compute topological indices, such as the relative rotation rates, of the periodic orbits in the strange attractor. We use the relative rotation rates of these orbits to determine their organization and to identify the windows in each region in the superstructure.

We also construct a two-dimensional return map for both the generic nonlinear oscillator and the Duffing oscillator. From this we construct one-dimensional return maps. Although a caricature of the dynamics, the one-dimensional return maps account very well for all features encountered so far in the bifurcation diagrams of nonlinear oscillators: superstructure (global torsion), primary structure (windows of Newhouse and dual orbits), fine structure (windows of other well-ordered orbits), and hyperfine structure (windows of non-well-ordered orbits).

One- and two-dimensional return maps have already been discussed for nonlinear oscillators in general and the Duffing oscillator in particular. Eilenberger and Schmidt [26] presented an algorithm for associating a two-dimensional map with the flow of a nonlinear oscillator. Parlitz *et al.* [27] observed the regularities in the bifurcation structure of a wide class of nonlinear oscillators and the similarities among them. They derived two-dimensional maps to simplify the study of these bifurcations. They were also able to assign topological indices to some of the bifurcation regions. Gilmore [28] and McCallum and Gilmore [19] suggested that a global understanding of the mechanisms underlying the observed regularities could be achieved at a topological level. In this picture the appropriate topological indices are the torsion, or flow around the direction of propagation of a periodic orbit, and the topological organization of pairs of periodic orbits. The torsion of a periodic orbit is a sum of two terms. The first term is an integer ("global torsion") which changes by ± 1 (± 2 for the Duffing oscillator) on passing from one bifurcation peninsula to an adjacent peninsula. The second is a rational fraction which can be computed from the symbolic dynamics of the corresponding orbit in the zero global torsion region of the bifurcation diagram. The topological organization of periodic orbits is determined by their mutual linking numbers and relative rotation rates. The purpose of the present work is to show that this suggestion is correct and show how it leads to a deeper understanding of the mechanisms responsible for the regularities observed in the bifurcation spectra of nonlinear oscillators in general and the Duffing oscillator in particular.

II. RANGE OF CONTROL PARAMETER VALUES

In the absence of driving and damping forces the Duffing oscillator is a conservative system obeying the equations of motion

$$d^2x/dt^2 = -\partial V/\partial x \ , \qquad V(x;a,b) = \tfrac{1}{4}x^4 + \tfrac{1}{2}ax^2 + bx \ . \tag{2.1}$$

The potential $V(x;a,b=0)$ is that of the symmetry restricted cusp catastrophe [29,30]. Depending on the value of the parameter a for $b=0$, three separate cases are encountered. For $a>0$ this potential is a single-well potential; for $a=0$ the well has a quartic shape with a triply degenerate critical point at the origin; for $a<0$ this is a double-well potential. If $a \neq 0$ the state variable can be rescaled so that $a=\pm 1$ and the symmetric potential assumes the form $x^4/4 \pm x^2/2$.

We will study the double-well potential. In the conservative case, the energy $E=(dx/dt)^2/2 + V(x;a=-1,b=0)$ is a constant of the motion. If $E<V(x=0;a=-1,b=0)=0$, the motion is confined either to the left-hand well or the right-hand well. If $E>0$ the motion extends over both wells. For $E=0$ the trajectory lies on one branch of a double homoclinic connection to the saddle at the origin $(x,dx/dt)=(0,0)$ in phase space.

We modify the motion in the usual way by introducing a time-dependent symmetry-breaking term in the potential and a velocity-dependent damping term in the dynamics:

$$V(x;a=-1,b(t)) = \tfrac{1}{4}x^4 - \tfrac{1}{2}x^2 - xb(t) \ , \qquad b(t) = b_0 \sin(2\pi t/T) \ . \tag{2.2}$$

The first-order equations of motion are

$$dx/dt = y \ , \qquad dy/dt = -\delta y - \partial V/\partial x = -\delta y + x - x^3 + b_0 \sin(2\pi t/T) \ . \tag{2.3}$$

The phase space for this dynamical system is $\mathbb{R}^2 \times S^1$.

These equations are invariant under the transformation $(x,y,t) \rightarrow (-x,-y,t+T/2)$. This means that if the point (x,y,t) in phase space is on an orbit of period p, the point $(-x,-y,t+T/2)$ must also be on an orbit of period p [12,31]. If the two points are on the same orbit, that orbit is called a symmetric orbit. If the two points are on distinct orbits, the two orbits are asymmetric. They form a symmetric (or symmetry-related pair) of asymmetric orbits. The projection of a symmetric orbit from the phase space $\mathbb{R}^2 \times S^1$ to the x-y plane $\mathbb{R}^2$ is invariant under rotations by π about the origin. This operation maps the projection of one asymmetric orbit into that of its partner.

We will develop a topological model for the behavior of (2.3) for a particular range of control parameter values.

(i) The strength of the driving term b_0 is chosen so that the potential (2.2) alternately becomes unimodel and bimodal during the drive cycle (Fig. 3). This requires $b_0^2 > 2^2/3^3$.

(ii) The damping per driving period will be held constant to emphasize the near periodicity of the bifurcation behavior as the drive period T is increased. Since the divergence of (2.2) is $-\delta$, the rate of volume contraction

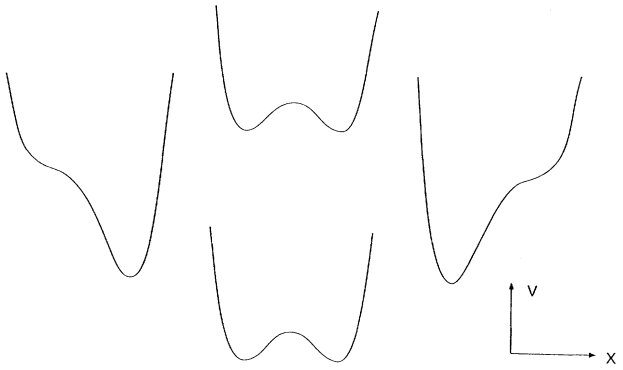

FIG. 3. The symmetry-breaking term $-xb_0\sin(2\pi t/T)$ alternately destroys the right-hand well and the left-hand well in the two-well Duffing potential. The shape of the potential is shown at four points on a cycle for $a=-1$ and $b=\frac{1}{2}$.

per period is $e^{-\delta T}$. We will choose $\delta=\varepsilon/T$ and hold ε constant, so that the volume contraction per period is fixed at $e^{-\varepsilon}$. Geometric models of the Duffing oscillator have previously been considered for small [6] and intermediate [32] values of the driving force.

III. DETERMINATION OF A TEMPLATE

A. Background

Roughly speaking, a template [22–25] is a two-dimensional structure, a branched manifold, which serves to model a flow which takes place in a strange attractor whose Lyapunov dimension is between 2 and 3. The flow can be projected to this two-dimensional manifold (for example, by increasing the dissipation) without modifying the topological organization of any of the periodic orbits in the flow. Templates are useful for visualizing the topological structure of the flow and for determining the organization of periodic orbits in the flow. They are used as an input for the computation of the topological indices (relative rotation rates and local torsions) which we use to identify the various windows in each region of the superstructure. We have determined a template for the Duffing oscillator, in the range of control parameter values described above, using a combination of numerical computation and intuitive insight [19,21].

Equations (2.3) were integrated to construct the bifurcation diagram shown in Fig. 2. For parameter values at which chaotic behavior is observed, the values $x,y,\phi=2\pi(t \bmod T)$ were stored. The structure of the attractor, in particular the stretching and squeezing mechanisms responsible for creating the attractor, was determined by investigating the cross section of the strange attractor on a Poincaré section P_ψ in the phase space $\mathbb{R}^2\times S^1$. The cross section was animated by sweeping the Poincaré section P_ψ through 2π rad. The results are summarized in Fig. 4 [19,21].

For fixed T the behavior of the animated cross section is as follows. After entering the left-hand well, the strange attractor has a roughly semicircular cross section. During the first half period, while motion is confined to the left-hand well, the arc rotates clockwise about the center of the well and elongates as it rotates. The number of rotations it makes while in the left-hand well is roughly $\frac{1}{2}T/\tau$, where τ estimates the natural period of the oscillator in the left-hand well. Since the well is not quadratic and the depth and location of the bottom vary over this half cycle, τ is not precisely defined. It is roughly 25% larger than 2π. When the left-hand well is destroyed by the time variation of the symmetry-breaking term in the potential, the cross section is "poured" into the right-hand well. In this process, the roughly circular shape of the cross section is compressed along a diameter, and on entering the right-hand well the cross section assumes the semicircular arc shape it exhibited, half a period earlier and rotated by half a turn, in the left-hand well. The rotation and elongation processes which occurred in the left-hand well are then repeated in the right-hand well, and at the end of the second half period, the cross section is poured back into the left-hand well. This process is repeated each period.

A useful intuitive visualization of this mechanism is as follows. Drip a semicircular arc of blue ink on the surface of white paint in a bucket of paint. Now stir the paint. The ink arc will rotate around the center of the surface, elongate, and become thinner. Now pour the paint into an empty bucket. If done carefully, during this pouring procedure the roughly circular elongated ink arc will be compressed as it flows out of the narrow channel of the tipped bucket and will assume a roughly semicircular arc shape on the surface in the second bucket. The process of stirring and pouring from bucket to bucket is then repeated, building up a fractal structure in the process.

B. Nonlinear oscillator template

In order to construct a template for the Duffing oscillator in this parameter regime, we first construct a template for a typical single-well nonlinear oscillator which exhibits the same evolution properties: free evolution with stretching and rotation, followed by squeezing along a diameter. This process is illustrated in Fig. 5. In Fig. 5(a) we show a schematic section of the strange attractor at the beginning of the rotating and stretching phase. Figure 5(b) is a representation of this cross section at the end of this phase. Figure 5(c) is a representation of the cross section after compression along a diameter. We have indicated only four branches of the template. The integer labels (0,1,2,3, . . .) are the local torsions of these branches, measured in units of π. This is the local torsion of the hyperbolic period-one orbit in that branch. The location of the period-one orbit in each branch is indicated by the symbol $\times$.

The template matrix associated with this template is obtained as follows [23]. The diagonal element $T(i,i)$ is the local torsion of the period-one orbit in branch i (namely, i). The off-diagonal elements $T(i,j)=T(j,i)$ are twice the linking numbers of the period-one orbits in branches i and j. $T(i,i)$ and $T(i,j)$ can be computed by

counting the number of half rotations made by a small vector at period-one orbit i, or a segment connecting period-one orbits i and j, on cycling through the two processes described in Fig. 5. The template matrix for the four branches shown in Fig. 5(b) is shown in Fig. 5(d). Below this matrix an array indicates the order in which these branches are joined after the squeezing process. By convention, clockwise rotations are negative. We will not display the negative signs, as all rotations encountered below are clockwise.

If the flow over the strange attractor is confined to branches 0 and 1 we recover the template for the zero-torsion horseshoe ("direct" horseshoe). If the motion is confined to branches 1 and 2 we have another horseshoe template ("reverse" horseshoe). If the motion is confined to branches 2 and 3 (or 4 and 5, . . .) the corresponding template differs from the zero-torsion direct horseshoe template by an additive global torsion N ($=1$ or $2, \ldots$). The corresponding template matrix is obtained by the substitutions $0 \rightarrow 2$, $1 \rightarrow 3$, and adding 2 to all template matrix elements. A similar relation exists for the reverse horseshoes on branches 1 and 2, 3 and 4, . . . [23].

To any periodic orbit on the zero-torsion direct horseshoe on branches 0 and 1 there exists a unique corresponding orbit on the direct horseshoe with global torsion N on branches $2N$ and $2N+1$. The symbolic dynamics of the corresponding orbits is related by $0 \leftrightarrow 2N, 1 \leftrightarrow 2N+1$.

As the control parameter T increases we expect a flow originally confined to branches 0 and 1 to be shifted over to branches 1 and 2, then 2 and 3, and so on. During this process we would expect the flow to extend over three

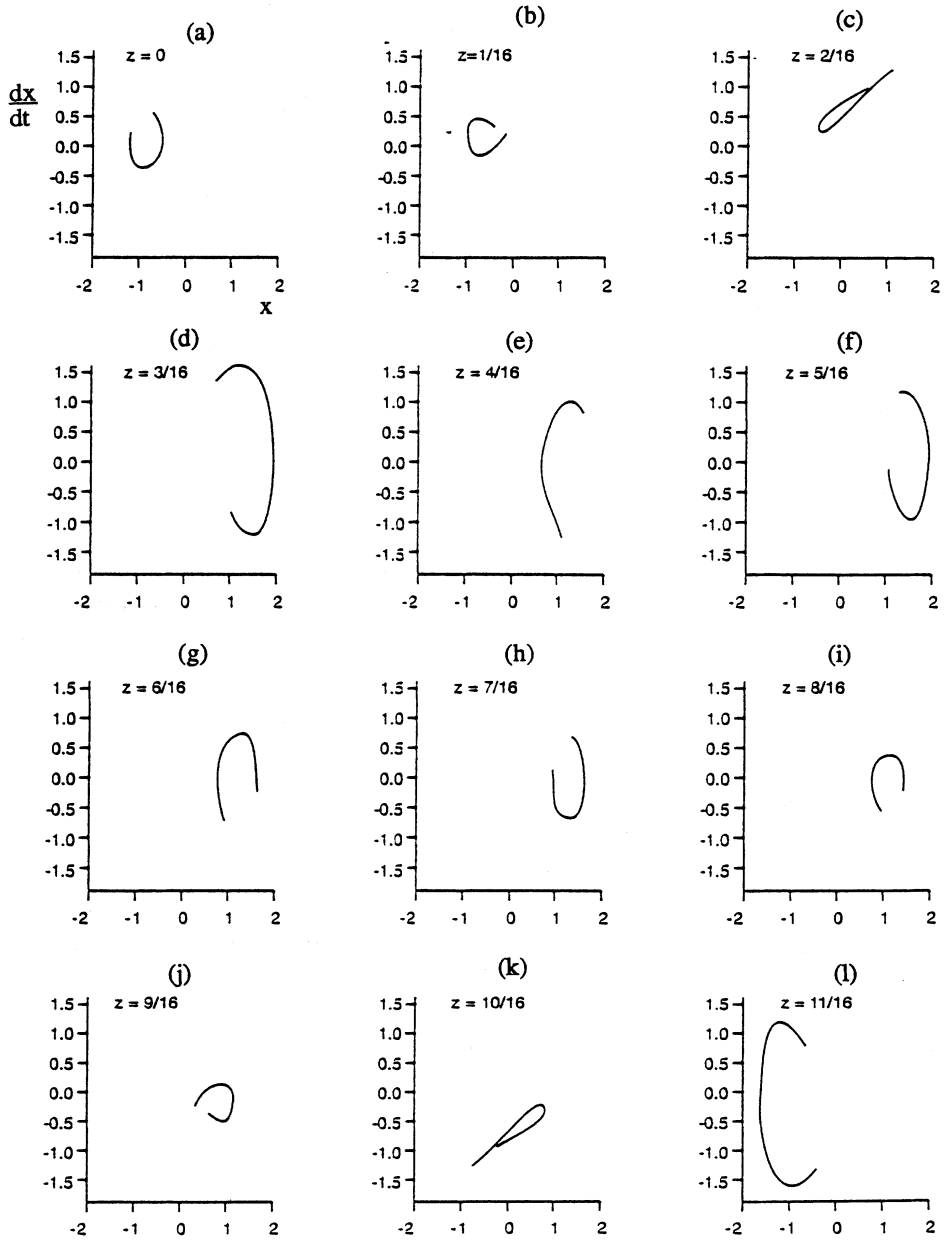

FIG. 4. This sequence of Poincaré sections shows the stretching and squeezing processes which combine to create the strange attractor of the Duffing oscillator. Each picture shows the strange attractor in a Poincaré section as the value of the phase $z_p = \psi/2\pi$ changes. The parameter values are $T = 30.5$, $b_0 = 1.0$, and $\varepsilon = 6.0$. In (a) $z_p = 0$ and z_p increases by $\frac{1}{16}$ in each successive section. (a)–(i) show the evolution of the attractor for one half period. The rotation and elongation phases are shown clearly in (d)–(j) and the process of pouring the attractor from one well to the other, squeezing in the process, is seen in (a)–(c) and again in (j)–(l).

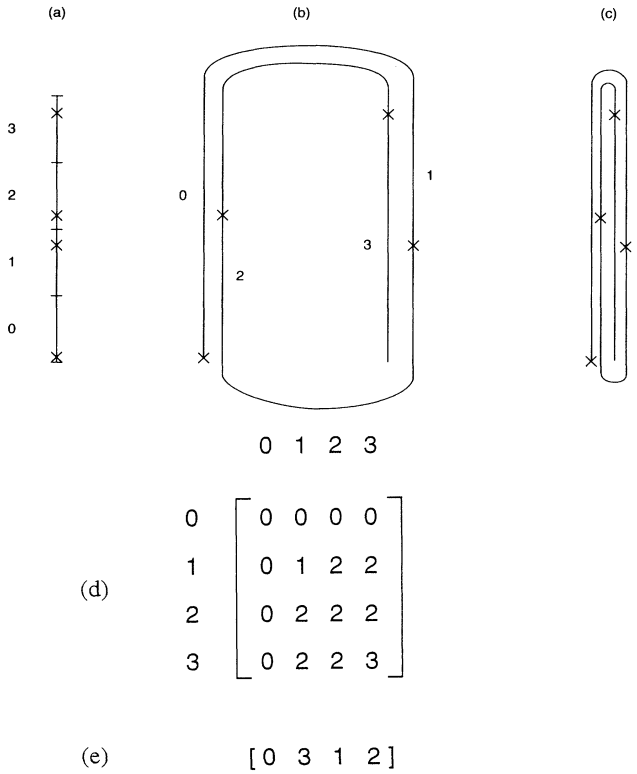

FIG. 5. (a) A set of initial conditions is (b) stretched and rotated around the bottom of the oscillator well and then (c) squeezed back into its initial configuration. The locations of the period-one orbits are indicated by ×'s. The template matrix (d) is determined by computing the number of half rotations in the neighborhood of each period-one orbit, $T(i,i)=i$, and the number of rotations by π of the segment connecting orbits i and j. This is twice the linking number of these two orbits $T(i,j)=T(j,i)=2L(i,j)$. The array (e) indicates the order in which the branches are squeezed together at the end of the stretching phase.

branches 0, 1, and 2, then 1, 2, and 3, . . . for some range of T. We investigate the morphology of this transition in more detail in Sec. VI.

C. Duffing template

The Duffing template, for the control parameter values under consideration, is deduced in much the same way as that of the generic nonlinear oscillator. The computation is outlined in Fig. 6. In Fig. 6(a) we show an arc of initial conditions in the left-hand well at the beginning of the half cycle during which that well exists. This set is divided into four large segments (0,1,2,3), each of which is subdivided into four smaller ones. Each small segment will become one branch of the final template.

As the dynamics evolves in the left-hand well, the arc shown in Fig. 6(a) will stretch and rotate, and as $t \to t+\frac{1}{2}T$ will have the shape shown in Fig. 6(b). At the end of this half period the left-hand well ceases to exist and the attractor enters the right-hand well. As it does so, the four large segments (0,1,2,3) are squeezed together and rotated through π rad, where this process is repeated another half period. Figure 6(c) shows the structure in the right-hand well before the stretching process begins. For ease of visualization, we have not included the clockwise rotation by π associated with the transition from the left- to the right-hand well in Fig. 6(c). In Fig. 6(d) we represent the structure of the attractor after stretching toward the end of the second half period. Each branch in this representation is described by two symbols, the first describing the number of half rotations in the left-hand well, the second the number of half rotations in the right-hand well. On completion of the second half cycle, the right-hand well is destroyed and the strange attractor is forced back into the left-hand well, once again being squeezed and rotated by π rad in the process. Once back in the left-hand well, it has the structure shown at the beginning of the cycle, Fig. 6(a).

The algebraic description of this template is determined as previously described. We indicate the period-one orbit in each branch of the template with the symbol ×. Neglecting for a moment the two clockwise rotations by π in passing back and forth between the wells, the diagonal template matrix elements $T(ij,ij)=i+j$ are the local torsions experienced in the two wells. The linking numbers $L(ij,kl)$ of the period-one orbits (ij) and (kl) are determined by counting how many rotations a vector connecting the two orbits makes during the sequence shown in Fig. 6: $a \to b \to c \to d \to a$. The off-diagonal matrix elements of the template matrix are twice the linking numbers of the corresponding orbits: $T(ij,kl)=2L(ij,kl)$. This is the rotation of the difference vector, measured in units of π during one full drive period. The template matrix constructed in this way is shown in Fig. 6(e). The array showing the order in which the branches are squeezed together in the passage from Fig. 6(d) $\to a$ is given below the template matrix [23]. To obtain the template matrix for the Duffing oscillator, we must also properly account for the two clockwise rotations by π in passing between the wells by adding 2 to all matrix elements. If more than four branches in each well are traversed, this algebraic description can easily be extended.

In order to describe the properties of periodic orbits it is useful to define the parity of each branch of a template as positive or negative depending on whether it is orientation preserving or reversing. The parity is the parity of the period-one orbit in that branch. This is $+1$ or -1 depending on whether its local torsion is even or odd. For the generic nonlinear oscillator, the parity of branch i is $(-1)^i$; for the Duffing template the parity of branch (ij) is $(-1)^{i+j}$. In either case, the parity of a periodic orbit is the product of the parities of the symbols constituting its symbolic dynamics.

IV. RELATIVE ROTATION RATES AND PERIODIC ORBITS

Relative rotation rates provide a useful tool for the analysis of periodic orbits in low-dimensional (phase space is three dimensional) dynamical systems [33]. They are easy to compute once periodic orbits have been identified in a dynamical system. They are also simple to

compute from their symbolic dynamics once a template describing a strange attractor, and all the periodic orbits associated with it, has been identified. They are topological invariants, independent of the dynamical stability of the orbits. Relative rotation rates will be used to identify the windows which appear in the bifurcation diagram of the Duffing and other nonlinear oscillators.

A. Review of relative rotation rates

Relative rotation rates were initially defined for periodically driven dynamical systems [33]. Two periodic orbits A and B of periods p_A and p_B intersect a Poincaré section at points A_i $(1 \le i \le p_A)$ and B_j $(1 \le j \le p_B)$. If we choose A_i and B_j as initial conditions and propagate the difference vector $A_i - B_j$ forward for $p_A p_B$ periods, this difference vector will return to its initial orientation by rotating through an integer number of full rotations in a plane transverse to the direction of motion. This integer multiple of 2π rad is the linking number of the two orbits of period $p_A p_B$ with initial conditions A_i and B_j. The relative rotation rate $\mathcal{R}_{ij}(A,B)$ for these initial conditions is the average number of rotations, per period, made by this difference vector. A relative rotation rate can be computed for each of the $p_A p_B$ pairs of initial conditions. The relative rotation rates of orbits A and B are the set of

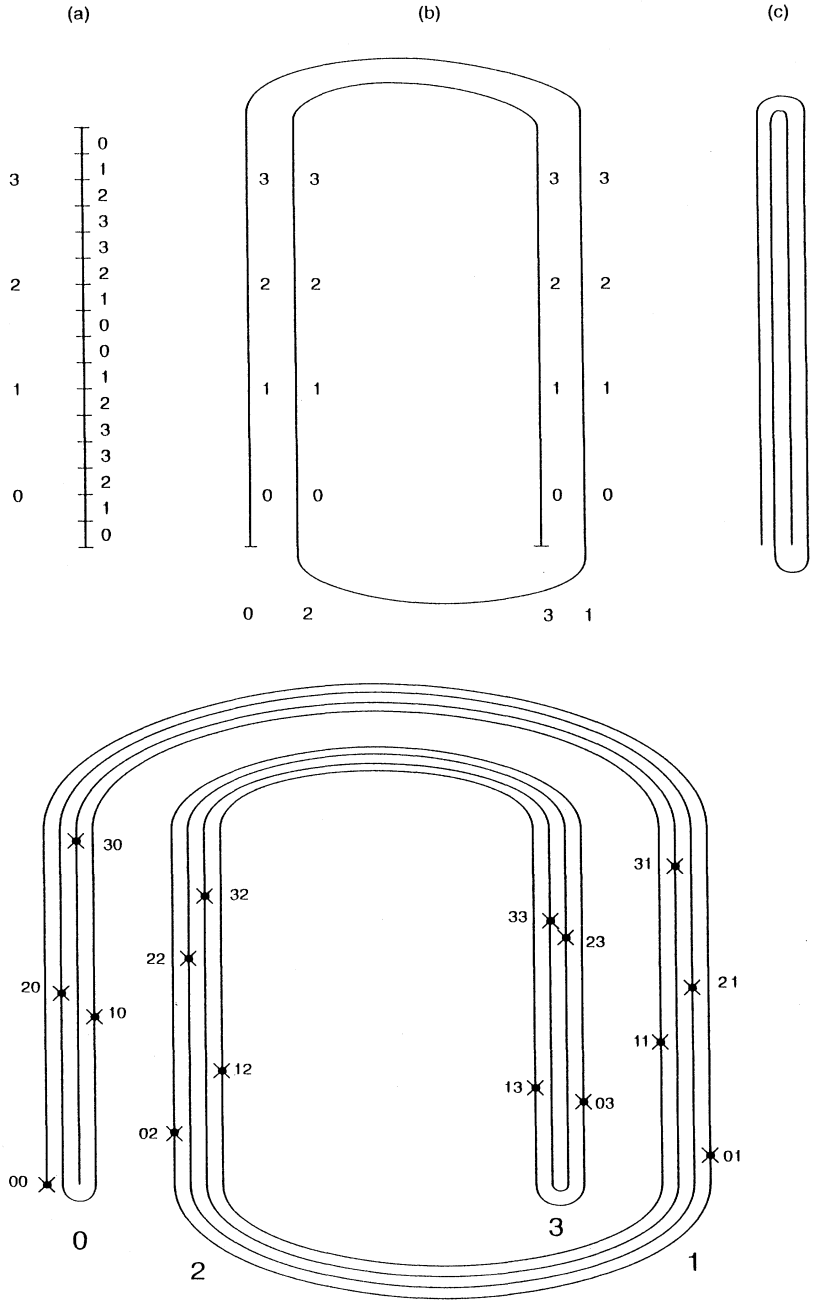

FIG. 6. The Duffing template is the second iterate of the template shown in Fig. 5. (a) A set of initial conditions in one well is (b) stretched and rotated around the bottom of that well. This structure is (c) squeezed along a diameter when "poured" from one well to another. After being stretched and rotated around the bottom of the second well, it has the structure shown in (d). The period-one orbit in each branch is shown ($\times$) and indicated by the branch label. The template matrix (e) is computed by determining the local torsion $T(ij,ij)=i+j$ in each branch and computing the linking number of each pair of period-one orbits (ij) and (kl). The integer 2 must be added to all matrix elements to properly account for the rotation through π rad experienced on passing from well to well. The array (f) indicates the order in which the branches are squeezed together.

		0				1				2				3			
		0	1	2	3	3	2	1	0	0	1	2	3	3	2	1	0
0	0	0	0	0	0	0	0	0	0	0	0	0	0	0	0	0	0
	1	0	1	2	2	2	2	2	2	2	2	2	2	2	2	2	2
	2	0	2	2	2	2	2	2	2	2	2	2	2	2	2	2	2
	3	0	2	2	3	4	4	2	2	2	2	4	4	4	4	2	2
1	3	0	2	2	4	4	4	2	2	2	2	4	4	4	4	2	2
	2	0	2	2	4	4	3	2	2	2	2	4	4	4	4	2	2
	1	0	2	2	2	2	2	2	2	2	2	4	4	4	4	2	2
	0	0	2	2	2	2	2	2	1	2	2	2	2	2	2	2	2
2	0	0	2	2	2	2	2	2	2	2	2	2	2	2	2	2	2
	1	0	2	2	2	2	2	2	2	2	3	4	4	4	4	4	4
	2	0	2	2	4	4	4	4	2	2	4	4	4	4	4	4	4
	3	0	2	2	4	4	4	4	2	2	4	4	5	6	6	4	4
3	3	0	2	2	4	4	4	4	2	2	4	4	6	6	6	4	4
	2	0	2	2	4	4	4	4	2	2	4	4	6	6	5	4	4
	1	0	2	2	2	2	2	2	2	2	4	4	4	4	4	4	4
	0	0	2	2	2	2	2	2	2	2	4	4	4	4	4	4	3
		0	15	5	11	9	8	13	4	1	14	5	10	9	7	13	2

FIG. 6. (*Continued*).

$p_A p_B$ relative rotation rates computed for each pair of initial conditions. The sum over all relative rotation rates of orbits A and B is the linking number $L(A,B)$ of orbits A and B:

$$\sum_{1\le i\le p_A}\ \sum_{1\le j\le p_B} \mathcal{R}_{ij}(A,B)=L(A,B)\ . \tag{4.1}$$

The (self-)relative rotation rates of an orbit with itself can also be computed. The self-relative rotation rates $\mathcal{R}_{ij}(A,A)$ $(i\neq j)$ are well defined. We define $\mathcal{R}_{ii}(A,A)=0$ to preserve the property that the sum over all (self-)relative rotation rates is the (self-)linking number of the orbits involved.

Relative rotation rates are topological invariants: they are unchanged under deformation of the dynamical system as long as the orbits exist. This allows us to compute their values in the hyperbolic limit, using a template, and then deform the system into a nonhyperbolic regime where saddle-node bifurcations and period-doubling cascades occur. Relative rotation rates have been used to identify the stretching and squeezing mechanisms responsible for generating strange attractors [24,25] to describe how a dynamical system evolves as control parameter values are changed [34], test models of physical systems [34,35], and to identify bifurcation peninsulas of the Duffing oscillator [12,14].

Relative rotation rates provide the following three pieces of information about periodic orbits on templates of the type shown in Fig. 5.

1. Well-ordered orbits. If all the nonzero self-relative rotation rates of an orbit are equal, the orbit is well ordered (a torus knot), and conversely [33]. For example, the important period-three orbit 001 is well ordered, since it has self-relative rotation rates $(1/3)^6,0^3$. Its saddle-node partner 011 has the same set of relative rotation rates. The largest windows in the bifurcation diagram of the Duffing oscillator, as well as their systematic organization, are due to stable well-ordered orbits. It is therefore useful to have a simple means to identify these orbits.

Non-well-ordered orbits [33,36,37] are not torus knots. They have positive topological entropy and force the presence of many other periodic orbits. Non-well-ordered orbits are easily identified by the spectrum of their nonzero self-relative rotation rates.

2. Local torsion [33,38–40]. When a periodic orbit A is created by saddle-node bifurcation, the intersections A_i on a Poincaré section are not close to each other, so self-relative rotation rates do not directly provide local information. However, if B is the saddle-node partner of A, the intersection B_i is near A_i. The mutual relative rotation rates of the saddle-node pair A and B then do provide local information. If A and its saddle-node partner B are well ordered, all mutual relative rotation rates are equal and their value is the local torsion of either orbit at creation. If the orbits are not well ordered, the local torsion is the mean value of their mutual relative rotation rates.

In a period-doubling cascade based on the period-one orbit (1, 01, 0111, 01110101, etc.) the local torsion of the orbit of period 2^k is the mean of the relative rotation rates of the mother-daughter pair of orbits of periods 2^k and 2^{k+1}: $(1/2,\ 1/4,\ 3/8,\ 5/16,\ 11/32,\ 21/64,\ \ldots=[2^k+(-1)^{k-1}]/3\times 2^k)$ [33].

For a saddle-node pair of period p, the orbit of period $p2^k$ is $\langle\mathcal{R}\rangle\pm[2^k+(-1)^{k-1}]/3p2^k$, where $\langle\mathcal{R}\rangle$ is the local torsion of the initial saddle-node pair and the sign is $+1$ on direct horseshoes (branches 0 and 1, 2 and 3, etc.) and -1 on reverse horseshoes (branches 1 and 2, 3 and 4, etc.) [33,41–44].

3. Concentric organization. The organization of periodic orbits can be determined by inspection of a table of their relative rotation rates. For example, the period-one orbit 1, the period-two orbit 01, and the period-three orbit 001 all have the same relative rotation rates with the period-four orbit 0001. This means that the period-two and -three orbits can be deformed to the period-one

orbit without intersecting the period-four orbit [33]. Another way to view this is that the period-one, -two, and -three orbits lie "inside" the period-four orbit. We find, by computation of relative rotation rates, that the orbits responsible for the largest windows in the bifurcation diagrams of the Duffing and other oscillators are concentrically organized in a very particular way which is model independent, depending only on their symbolic dynamics [37].

B. Periodic orbits for nonlinear oscillators

Three types of orbits play a major role in understanding the bifurcation diagram of the Duffing oscillator: the initial period-doubling sequence; well-ordered saddle-node pairs; and the period-doubling cascade based on the well-ordered node. We describe these orbits first for the generic nonlinear oscillator on the horseshoe consisting of the branches (0,1) of the template shown in Fig. 5 (direct horseshoe). We then describe these orbits on the horseshoe consisting of the branches (1,2) of this template (reverse horseshoe). Finally, we describe these orbits on higher horseshoes.

1. Direct horseshoe (0,1 template branches)

The initial period-doubling cascade consists of the saddle 0 and the node 1, on which the cascade (1, 01, 0111, 01110101, etc.) is based with local torsions $[2^k+(-1)^{k-1}]/3\times 2^k$, computed from their relative rotation rates.

All well-ordered orbits in this horseshoe are identified by an irreducible rational fraction Q/P, with P the period and $0<Q/P<1/2$. The symbol sequence $\mathcal{S}(Q/P)$ for the saddle of this saddle-node pair is $\mathcal{S}(Q/P)=W(1)W(2)\ldots W(P-Q)$,

$$W(j)=\begin{cases}0 & \text{if } [fj]-[f(j-1)]=0\\ 11 & \text{if } [fj]-[f(j-1)]=1\end{cases}, \tag{4.2}$$

where $f=Q/(P-Q)$, $[x]$ is the greatest integer in x, and $j=1,2,\ldots,P-Q$ [33,37]. The node of this saddle-node pair is obtained by changing $W(P-Q)$ from 11 to 01. For example, the saddle-node pair associated with the fraction $Q/P=3/7$ is $\mathcal{S}(3/7)=(0\,11\,11\,\underline{1}1)$ and the saddle-node pair identified by 1/7 is $\mathcal{S}(1/7)=(00000\,\underline{1}1)$, where $\underline{1}$ is 1 for the saddle and 0 for the node. All nonzero relative rotation rates of the well-ordered orbits identified by Q/P are Q/P. Further, all their mutual relative rotation rates are also Q/P, so that their local torsion is Q/P when formed by saddle-node bifurcation.

In Table I we show the relative rotation rates for the five well-ordered orbits with $Q/P=3/7,2/5,1/3,1/4,1/5$ [45]. This table clearly shows that these well-ordered orbits are concentrically organized, those with larger Q/P inside those with smaller. More generally, the relative rotation rates of well-ordered orbits with fractions Q/P and Q'/P' are

$$\mathcal{R}_{ij}(Q/P,Q'/P')=\min(Q/P,Q'/P') . \tag{4.3}$$

This shows that all well-ordered orbits are concentrically organized, those with smaller Q/P outside those with larger [37].

TABLE I. Relative rotation rates of five well-ordered orbits. The relative rotation rates of the distinct orbits with Q/P and Q'/P' are all equal and have multiplicity PP'. The self-relative rotation rates of an orbit with Q/P are $(Q/P)^{P(P-1)}0^P$. The underlined symbol $\underline{1}$ is 0 for the node and 1 for the saddle of the saddle-node pair. The structure of this table shows that these orbits are concentrically organized, with local torsion decreasing from inside to outside.

Q/P \ Q'/P'	3/7	2/5	1/3	1/4	1/5
	0 11 11 $\underline{1}$1	0 11 $\underline{1}$1	0 $\underline{1}$1	00 $\underline{1}$1	000 $\underline{1}$1
3/7	0 11 11 $\underline{1}$1	3/7	2/5	1/3	1/4	1/5
2/5	0 11 $\underline{1}$1	2/5	2/5	1/3	1/4	1/5
1/3	0 $\underline{1}$1	1/3	1/3	1/3	1/4	1/5
1/4	00 $\underline{1}$1	1/4	1/4	1/4	1/4	1/5
1/5	000 $\underline{1}$1	1/5	1/5	1/5	1/5	1/5

If Q/P and Q'/P' are irreducible rational fractions with $QP'-Q'P=\pm 1$, then there is a well-ordered orbit of period $P+P'$ between the two well-ordered orbits with Q/P and Q'/P'. Its properties are obtained from those of the two bounding orbits by "Farey construction." Its rational fractional value is obtained by "Farey addition" of the rational fractions Q/P and Q'/P': $Q''/P''=Q/P+_FQ'/P'=(Q+Q')/(P+P')$. The symbol sequence for this Farey orbit is obtained from the symbol sequence of the two bounding orbits

$$\mathcal{S}((Q+Q')/(P+P'))$$
$$=\mathcal{S}((\min(Q/P,Q'/P'))\mathcal{S}((\max(Q/P,Q'/P')) . \tag{4.4}$$

For example, between the Newhouse orbits 1/3 (011) and 1/4 (0011) there is a well-ordered orbit with $Q''/P''=1/3+_F1/4=2/7$ and symbol sequence $\mathcal{S}(2/7)=\mathcal{S}(1/4)\mathcal{S}(1/3)=0011\underline{1}1$.

A period-doubling cascade is built on the node of each saddle-node pair (well ordered or not). As stated above, the local torsion on this cascade reproduces that on the fundamental period-doubling cascade:

$$(\text{local torsion})=\langle\mathcal{R}\rangle+[2^k+(-1)^{k-1}]/3P2^k , \tag{4.5}$$

where P is the period of the basic saddle-node pair.

The largest windows in the bifurcation set are associated with the simplest well-ordered orbits. We identify the primary series of orbits as follows.

(a) Primary series (first half). For these orbits $Q/P=n/(2n+1)$ $(n=1,2,\ldots)$ and the symbolic dynamics is 01^{2n} (saddle) and $01^{2n-2}01$ (node). These orbits are anchored by the period-three orbit at one end and have local torsion accumulating, as $n\to\infty$, to 1/2.

(b) Primary series (second half). For these orbits $Q/P=1/n$ $(n=3,4,\ldots)$ and the symbolic dynamics is $0^{n-1}1$ (node) and $0^{n-2}1^2$ (saddle). These orbits are anchored by the period-three orbit at one end and have local torsion accumulating, as $n\to\infty$, to 0. These orbits have been studied extensively by Newhouse [20]. These orbits are dual under the transformation $0\to 1^2$ [e.g., $1/5=0^31^2\to 3/7=(1^2)^30=01^{2\times 3}$].

The five orbits shown in Table I belong to the first half

of the primary series (3/7,2/5,1/3) and the second half of the primary series (1/3,1/4,1/5). The local torsions Q/P of both the first and the second half of the primary series can be constructed by Farey addition from the local torsion (1/3) of the period-three orbit which anchors both halves and the two accumulation values on the left (1/2), associated with symbol sequence $\mathcal{S}(1/2)=(11)$, and 0/1 on the right, associated with symbol sequence $\mathcal{S}(0/1)=(0)$. This construction is shown in Fig. 7. In the first half of the primary series the Farey orbit between 1/2 and 1/3 is 2/5 with $\mathcal{S}(2/5)=\mathcal{S}(1/3)\mathcal{S}(1/2)=(011)(11)$; that between 1/2 and 2/5 is 3/7 with $\mathcal{S}(3/7)=\mathcal{S}(2/5)\mathcal{S}(1/2)=(01111)(11)$, etc. Thus the first half of the primary series is dominated by the flip saddle 1 whose local torsion is 1/2. Similarly, in the second half of the primary series the Farey orbit between 1/3 and 0/1 is 1/4 with $\mathcal{S}(1/4)=\mathcal{S}(0/1)\mathcal{S}(1/3)=(0)(011)$, etc. The second half of the primary series is dominated by the regular saddle 0, whose local torsion is 0.

Between each adjacent pair of windows in the primary structure there is a fine structure of windows associated with well-ordered orbits. These orbits can be built up sequentially by Farey construction. Figure 8 shows the fine structure between windows 1/3 and 1/4 down to level 3. The orbit with $Q/P=2/7$ is the well-ordered orbit of lowest period which does not belong to the primary series. The well-ordered orbits $\mathcal{S}(1/3)=011$ and $\mathcal{S}(1/4)=0011$ dominate the behavior of all Farey orbits between these windows in the same way the orbits $\mathcal{S}(1/2)=11$ and $\mathcal{S}(1/3)=011$ [or $\mathcal{S}(1/3)$ and $\mathcal{S}(0/1)$] dominate the behavior of all primary orbits in the first (second) half of the primary series.

LOCAL TORSION

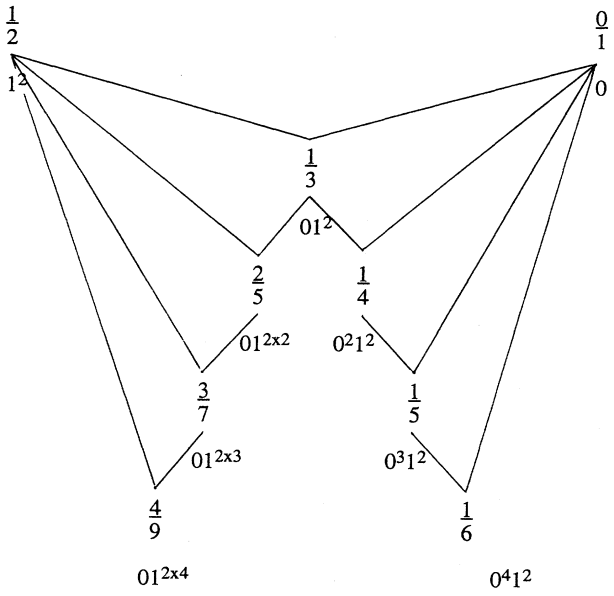

FIG. 7. Each well-ordered orbit in the first half of the primary series can be constructed sequentially as the Farey sum of the orbit 011 with $Q/P=1/3$ and the limit orbit 1^2. Likewise, each Newhouse orbit in the second half of the primary series is constructed sequentially as the Farey sum of the period-three orbit 011 and the limit orbit 0. The two period-one orbits 1 and 0 dominate the first and second halves of the primary series of orbits. At any level there is a duality between orbits: $0(1^2)^p$ is dual to 0^p1^2.

LOCAL TORSION

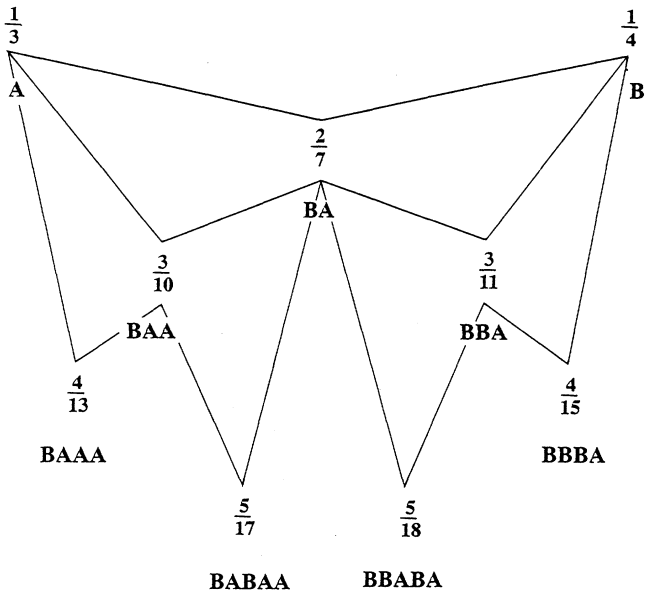

FIG. 8. Each well-ordered orbit between two adjacent windows in the primary series can be obtained from the boundary orbits by Farey construction. Some of the well-ordered orbits between the windows 1/3 and 1/4 are shown. Here $A=011$ and $B=0011$.

Scattered throughout the bifurcation diagram between primary windows and the fine structure, extending even beyond the accumulation point of the first half of the primary series, is a set of very narrow windows associated with non-well-ordered orbits. The non-well-ordered orbit of lowest period in this horseshoe is the period-five orbit with symbolic dynamics 00111, mutual relative rotation rates $(1/5)^{15}(2/5)^{10}$, and $\langle\mathcal{R}\rangle=7/25$. For highly dissipative nonlinear oscillators, the very narrow window created when this orbit is formed by saddle-node bifurcation will occur in the neighborhood of the window of the well-ordered orbit with $Q/P=7/25$, which is the Farey sum of 2/7 and 5/18 (cf. Fig. 8). From Fig. 8 we easily compute the symbolic dynamics of this well-ordered orbit as $\mathcal{S}(7/25)=\mathcal{S}(5/18)\mathcal{S}(2/7)=(BBABA)(BA)=B(BA)^3=0011(0011011)^3$.

2. Reverse horseshoe (1,2 template branches)

Every orbit that exists on the horseshoe formed on branches 0,1 of the template shown in Fig. 5 has a counterpart on the reverse horseshoe formed on branches 1,2 of this template. The mapping between orbits on the

direct horseshoe and the reverse horseshoe is as follows.

(a) Symbol mapping: $1\rightarrow 1$, $0\rightarrow 2$.

(b) All relative rotation rates are complemented in 1: $\mathcal{R}\rightarrow 1-\mathcal{R}$.

(c) All local torsions are complemented in 1.

For example, the Newhouse orbits $0^{p-2}1^2, 0^{p-1}1$ on the direct horseshoe are identified with the Newhouse orbits $2^{p-2}1^2$, $2^{p-1}1$ in the reverse horseshoe. Their self- and mutual relative rotation rates are $1-1/p$. These well-ordered orbits are concentrically organized since

$$\mathcal{R}_{ij}(1-Q/P,1-Q'/P')=\max(1-Q/P,1-Q'/P') =\min(Q/P,Q'/P') . \quad (4.6)$$

The local torsions on period-doubling cascades are $\langle\mathcal{R}\rangle-[2^k+(-1)^{k-1}]/3P2^k$.

3. *Higher horseshoes (branches 2N, 2N+1, and 2N+2)*

The direct horseshoe formed by branches $2N$ and $2N+1$ is identical to that formed by the direct horseshoe built on branches 0 and 1, except for an overall global torsion of N. The following mapping takes the zero-torsion horseshoe (on branches 0,1) and its orbits to the corresponding direct horseshoe ($2N$, $2N+1$) and its corresponding orbits.

(a) Symbol replacement: $0\rightarrow 2N$, $1\rightarrow 2N+1$.

(b) Relative rotation rates: add N to each.

The reverse horseshoe formed on the branches $2N+1$ and $2N+2$ is identical to the reverse horseshoe built on branches 1 and 2, except for an overall global torsion of N. We have the following mapping between these two reverse horseshoes.

(a) Symbol replacement: $1\rightarrow 2N+1$, $2\rightarrow 2N+2$.

(b) Relative rotation rates: add N to each.

To illustrate, the Newhouse orbits of period p on the reverse zero-torsion horseshoe are 1^22^{p-2} and 12^{p-1} with self- and mutual relative rotation rates $1-1/p$. The corresponding orbits on the reverse horseshoe on branches 5 and 6 of the nonlinear oscillator template are 5^26^{p-2} (saddle) and 56^{p-1} (node) and their self- and mutual relative rotation rates are $2+(1-1/p)$.

C. Periodic orbits for the Duffing oscillator

Since the Duffing template (Fig. 6) is the second iterate of the template for a nonlinear oscillator (Fig. 5), orbits of period p of the Duffing oscillator may be represented as a sequence of $2p$ symbols in the form $(a_1a_2)(a_3a_4)\ldots(a_{2p-1}a_{2p})$, where a_j is a symbol for the nonlinear oscillator template in either the left- (j odd) or the right- (j even) hand well. An orbit is symmetric if the symbol sequence $(a_{p+1}a_{p+2})(a_{p+3}a_{p+4})\ldots a_1a_2\ldots(a_{p-1}a_p)$ is the same as the sequence $(a_1a_2)(a_3a_4)\ldots(a_{2p-1}a_{2p})$. Only orbits with negative parity can undergo period-doubling bifurcations.

If motion in each of the two wells of the Duffing oscillator is confined to branches 0 and 1, orbits for the Duffing oscillator are constructed from the four symbols (00), (01), (10), and (11). The period-one orbits (00) and (11) are symmetric with even parity. Therefore the node (11) cannot initiate a period-doubling cascade. The two period-one orbits (01) and (10) form a symmetric pair of asymmetric orbits. Since they have odd parity, they can initiate period-doubling cascades. The symmetric period-one orbits (00) and (11) are formed in a saddle-node bifurcation and then the stable node undergoes a pitchfork bifurcation, losing its stability and creating the asymmetric pair of orbits:

$$\underset{\text{stable symmetric}}{(11)} \longrightarrow \underset{\text{pitchfork bifurcation}}{(11)} + \underset{\text{unstable symmetric}}{(01)+(10)} \quad \underset{\text{stable symmetric pair of asymmetric orbits}}{.} \quad (4.7)$$

The two period-two orbits in this cascade are obtained from the period-four orbit 0111 on the oscillator template (01)(11) and (11)(01). The period-doubling bifurcations are

$$\begin{aligned}(01)&\rightarrow(01)(11) ,\\ (10)&\rightarrow(11)(10) .\end{aligned} \quad (4.8)$$

The symbolics for the two orbits of period 2^k in the Duffing cascade are obtained in this way from the symbolics of the single orbit of period 2^{k+1} in the oscillator cascade.

If motion is confined to N branches in each well of the Duffing oscillator, the template has N^2 branches. There are many more orbits of period p on this template than on the corresponding N-branched oscillator template. However, there is only a small subset of orbits in the Duffing system which are responsible for the primary and fine structure, which is evident in the Duffing bifurcation diagram (Fig. 2). These orbits are second iterates of the well-ordered and period-doubled orbits of the generic nonlinear oscillator with symbolic dynamics $(a_1a_2\ldots a_p)^2$, where $a_1a_2\ldots a_p$ is a well-ordered or period-doubled orbit for the nonlinear oscillator.

Two distinct cases arise when a Duffing orbit is the second iterate of an oscillator orbit: $(a_1a_2\ldots a_p)^2$. If p is odd, the Duffing orbit is symmetric. It also has even parity, so it cannot undergo a period-doubling bifurcation. If p is even, then $(a_1a_2\ldots a_p)$ is a Duffing orbit of period $p/2$, as is the shifted orbit $(a_2a_3\ldots a_pa_1)$. These orbits form a symmetric pair of asymmetric orbits. If their parity is odd they can initiate period-doubling cascades. We illustrate these two cases by using as examples second iterates of Newhouse orbits on the branches 0,1 of the oscillator template.

Example 1 (p odd). The two Newhouse orbits of period three on the oscillator template are 011 (saddle) and 001 (node). The second iterates on the Duffing template are $(011)^2=(01)(10)(11)$ (saddle) and $(001)^2=(00)(10)(01)$ (node). Both are symmetric. The node undergoes a symmetry-breaking bifurcation to a symmetric pair of asymmetric period-three orbits with symbolic dynamics (00)(10)(11) and (01)(01)(10), derived from the period-six daughter orbit 001011 on the oscillator template. Both of these orbits initiate a period-doubling cascade.

Example 2 (p even). The two Newhouse orbits of

period four are 0011 (saddle) and 0001 (node). The second iterate of the saddle gives two saddles of period two: $(0011)^2=(00)(11)(00)(11)=[(00)(11)]^2$ and $(0110)^2=(01)(10)(01)(10)$, while the second iterate of the node gives two nodes of period two: $(0001)^2=(00)(01)(00)(01)$ and $(0010)^2=(00)(10)(00)(10)$. The saddle-node pairs are $((00)(11),(00)(01))$ and $((01)(10),(00)(10))$. The node in each pair then initiates a period-doubling cascade.

The second iterate of the well-ordered orbit on the horseshoe on branches (0,1) defined by the rational fraction Q/P is a well-ordered orbit on the Duffing template. Its nonzero self- and mutual relative rotation rates are $1+2Q/P$. The relative rotation rates of Duffing orbits constructed from orbits with Q/P and Q'/P' on this horseshoe are

$$\mathcal{R}_{ij}(Q/P,Q'/P')=\min(1+2Q/P,1+2Q'/P') \ . \qquad (4.9)$$

Thus these Duffing orbits are also concentrically organized.

A similar construction holds for the reverse horseshoe on branches (1,2) of the oscillator template. The relative rotation rates of the Duffing orbits are $1+2(1-Q/P)$ and two such well-ordered orbits have relative rotation rates given by

$$\mathcal{R}_{ij}(1-Q/P,1-Q'/P') =\max[1+2(1-Q/P),1+2(1-Q'/P')] \ . \qquad (4.10)$$

Similar results hold for second iterates of orbits on branches $2N$, $2N+1$ and $2N+1$, $2N+2$ of the oscillator template. The relative rotation rates are $1+2(N+Q/P)$ and $1+2(N+1-Q/P)$, respectively.

D. Topological identification of the Duffing windows

We have identified the periodic orbits responsible for the largest windows in the bifurcation diagram of the Duffing oscillator. The symbolic dynamics of these orbits were determined by locating the position of successive iterates in Poincaré sections separated by half a period and comparing these positions with branches of the strange attractor at nearby control parameter values (i.e., just outside the window). This was done for orbits of periods three, five, and seven and orbit pairs of periods two and four in two separate regions of the bifurcation superstructure [21].

TABLE II. Relative rotation rates in the largest windows of the Duffing oscillator in the bifurcation diagram shown in Fig. 2. The largest windows are labeled by the integer p (3,4,. . .). For p odd there is a saddle-node pair of orbits of period p. For p even there are two saddle-node pairs of period $p/2$. The symbolic dynamics of these orbits are shown. The local torsions of the orbits are $7-2/p$. All relative rotation rates are the same for any pair of orbits. The nonzero self-relative rotation rates only are shown. The multiplicities are as indicated in Table I. The structure of this table shows that these orbits are concentrically organized.

p Symbolics	p' Local torsion	3 $7-2/3$	4 $7-2/4$	5 $7-2/5$	6 $7-2/6$	7 $7-2/7$	8 $7-2/8$
3 (56)(65)(66)		19/3	26/4	33/5	40/6	47/7	54/8
(55)(65)(66)							
4 (55)(66)							
(56)(66)							
		26/4	26/4	33/5	40/6	47/7	54/8
(56)(65)							
(55)(65)							
5 (55)(66)(65)(56)(66)		33/5	33/5	33/5	40/6	47/7	54/8
(56)(66)(65)(66)(66)							
6 (55)(66)(66)							
(56)(66)(66)							
		40/6	40/6	40/6	40/6	47/7	54/8
(56)(66)(65)							
(66)(66)(65)							
7 $(55)(66^2)65)(56)(66)^2$		47/7	47/7	47/7	47/7	47/7	54/8
$(56)(66)^2(65)(66)(66)^2$							
8 $(55)(66)^3$							
$(56)(66)^3$							
		54/8	54/8	54/8	54/8	54/8	54/8
$(56)(66)^2(65)$							
$(66)(66)^2(65)$							

In one region, orbits which we identified all had the form $(3^2 4^{p-2})^2$, $p=3,4,\ldots,8$. In the adjacent region the corresponding windows were associated with orbits $(5^2 6^{p-2})^2$, $3 \le p \le 8$. We computed all relative rotation rates for the orbits in these two regions of the superstructure. The self-relative rotation rates of the orbits in these two regions were $1+2(2-1/p)=5-2/p$ and $1+2(3-1/p)=7-2/p$. Table II gives the relative rotation rates for the orbits in the second region. These orbits are concentrically organized.

In the second region the local torsions are (19/3,26/4, 33/5,40/6,47/7,54/8) for $p=3,4,5,6,7,8$. This sequence of local torsions has also been identified by Englisch and Lauterborn [18]. However, these authors have not identified the orbits by their type or symbolic dynamics. The next two largest windows "on the other side" of the period-three window have local torsion 31/5 and 43/7.

The major windows in the bifurcation diagram of the Duffing oscillator are associated with well-ordered orbits, which are second iterates of Newhouse orbits on reverse horseshoe templates. Their symbolic dynamics are $(1^2 2^{p-2})^2$, $(3^2 4^{-2})^2$, $(5^2 6^{p-2})^2, \ldots$. Their self-relative rotation rates and local torsions are $1+2(N+1-1/p)$ and they are concentrically organized.

V. RETURN MAPS

The description of periodic orbits in terms of their symbolic dynamics on the nonlinear oscillator and Duffing templates has been extremely useful. So also has the description of these orbits in terms of their relative rotation rates, local torsions, and concentric organization. However, these properties are all "static," in the sense that they do not tell us directly about how periodic orbits are created and annihilated as control parameters traverse a bifurcation peninsula. To resolve this problem of "dynamics" we construct return maps for the nonlinear and Duffing oscillators. These maps are then used, to the extent possible, to determine the order in which periodic orbits are created and annihilated as a control parameter is varied. We have used the one-dimensional return map (5.4) to outline the bifurcation peninsulas shown in Fig. 1 for a typical nonlinear oscillator. This has been done by identifying the loci of saddle-node bifurcations of the period-three orbit in the (λ, T) plane for successively increasing values of the global torsion.

A. Two-dimensional return maps

The dynamical processes of stretching and squeezing that occur in the Duffing oscillator can be summarized by a two-dimensional return map. This map involves two steps in each well. The first describes the result of rotation and elongation in the left-hand well. The second describes the squeezing which occurs when the left-hand well is destroyed and the attractor is poured into the right-hand well. Steps 3 and 4 repeat steps 1 and 2 for the right-hand well. The first two steps provide a return map for typical nonlinear oscillators, such as the Morse and Toda oscillators, in a comparable range of parameter values. These four steps are summarized in Fig. 9.

Step 1. A point in the left-hand well with coordinates r,θ slowly spirals down toward the bottom of the well during the first half period. The angle θ is measured from the fiducial marker shown. The region of phase space shown in the strip between $\theta=0$ and π evolves to the strip between $\theta=\phi$ and $\phi+\lambda\pi$ under the mapping

$$\begin{aligned} &\text{SL1:}\quad \theta_0 \to \theta_1 = \phi + \lambda\theta_0 \ , \\ &\qquad r_0 \to r_1 = r_0 e^{-\gamma(\theta_1-\theta_0)} \ . \end{aligned} \tag{5.1}$$

In order for the strips shown to be nonoverlapping, we require $b > ae^{-2\pi\gamma}$.

Step 2. A circle of radius a containing the spiraling motion in the left-hand well is compressed along a diameter, rotated clockwise through π rad, and injected into the strip extending from 0 to π in the right-hand well. The point with coordinates (x,y) in the left-hand well is mapped to the point with coordinates (r_2,θ_2) in the right-hand well under the mapping

$$\begin{aligned} &\text{SL2:}\quad x = r_1\cos\theta_1 \ , \\ &\qquad y = r_1\sin\theta_1 \ , \\ &\qquad \theta_2 = \tfrac{1}{2}(\xi_1+\xi_2) + \tfrac{1}{2}(\xi_1-\xi_2)(x/a) \ , \\ &\qquad r_2 = [\tfrac{1}{2}(a+b) + \tfrac{1}{2}(a-b)(y/a)]e^{-\gamma\theta_2} \ . \end{aligned} \tag{5.2}$$

Steps 3 and 4 repeat steps 1 and 2 in the right-hand well.

The two-dimensional map SR2∘SR1∘SL2∘SL1 (here ∘ denotes composition of maps) provides a reasonable approximation to the periodic orbit structure and strange attractors of the Duffing oscillator. The first two steps

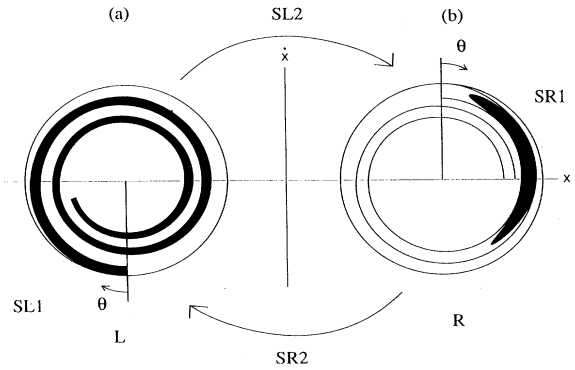

FIG. 9. Two-dimensional return map for the Duffing oscillator. (a) SL1: A point in the left-hand well with coordinates (r_0,θ_0) evolves to (r_1,θ_1) under free evolution given by (5.1). Points initially in the exponentially decaying strip in the region $0 \le \theta_0 \le \pi$ evolve to points in the strip shown. Here $b/a=0.89$ and $\gamma=0.04$. (b) SL2: Points with coordinates (r_1,θ_1) or (x,y) in the left-hand well are squeezed into the right-hand well, where their coordinates (r_2,θ_2) in the new local coordinate system are given by (5.2). The image of the disk $r \le a$ in the left-hand well is shown, in black, in the interior of the exponentially decaying strip in the right-hand well. Here $\xi_1=0.1\pi$ and $\xi_2=0.8\pi$. The two maps SL2∘SL1 form the return map of a generic nonlinear oscillator. The second iterate SR2∘SR1∘SL2∘SL1 forms the return map of the Duffing oscillator. The two rotations by π rad in passing between wells is taken into account by the orientations of the local coordinate systems.

SL2∘SL1 do the same for generic nonlinear oscillators. However, this map has six "unfolding" parameters: $\phi \sim \frac{1}{2}T/\tau$, λ (approximately equal to the square root of the Lyapunov exponent) b/a and γ, related to the dissipation, and the angular bounds on reinjection ξ_1, ξ_2. We have not studied this map thoroughly because of the large number of parameters. Rather, we have developed a one-dimensional return map which provides a very convenient basis for understanding almost all of the details previously seen in the structure of the bifurcation diagram of the Duffing oscillator.

B. One-dimensional return maps

This map is developed under the assumption that the intersection of the strange attractor with a Poincaré section is very "thin" ($a=b$), so that fractal structure is neglected. We assume that the location of a point in a cross section of the attractor is defined by an angle θ during each half period and neglect the slow spiral decay toward the well bottom ($\gamma=0$). We further assume that the angle θ ranges between 0 and π in each well at the beginning of each half period ($\xi_1=0, \xi_2=\pi$). The one-dimensional return map is then

$$\begin{aligned} &\theta_L \to \theta'_L = \phi + \lambda\theta_L \ , \\ &\theta'_L \to \theta_R = \pi/2(1-\cos\theta'_L) \ , \\ &\theta_R \to \theta'_R = \phi + \lambda\theta_R \ , \\ &\theta'_R \to \theta''_L = \pi/2(1-\cos\theta'_R) \ . \end{aligned} \tag{5.3}$$

From (5.3) we construct the first return map R^1 for generic nonlinear oscillators and the return map $R^2 = R^1 \circ R^1$ for the Duffing oscillator:

$$\begin{aligned} &R^1: \ \theta \to \theta' = \pi/2[1-\cos(\phi+\lambda\theta)] \ , \\ &R^2 = R^1 \circ R^1: \ \theta \to \theta'' \\ &\qquad = \pi/2(1-\cos\{\phi + \lambda\pi/2[1-\cos(\phi+\lambda\theta)]\}) \ . \end{aligned} \tag{5.4}$$

We first study the properties of the map R^1 because many of the features exhibited by R^2 for the highly dissipative Duffing system first become apparent in R^1. Then we describe how to construct R^2 as the second iterate of R^1.

C. Properties of R^1

We observe that for the map R^1 for generic nonlinear oscillators, $\phi(=2\pi T/\tau)$ is essentially the ratio of the driving period to the natural period of the linearized oscillator and λ is essentially the Lyapunov exponent of the map, or the unstable Lyapunov exponent of the flow. The return map is a trigonometric function with minima at $\theta'=0$ and maxima at $\theta'=\pi$. Between adjacent maxima and minima the map is monotonic. It is convenient to label each branch of this return map between adjacent maxima and minima with an integer: $i=[(\phi+\lambda\theta)/\pi]$. Then if $0<\phi+\lambda\theta<\pi$, θ lies under the $i=0$ branch of the return map, which is monotonic increasing from 0 to π. The next branch 1 descends from $\theta'=\pi$ to 0 and maps θ in the interval $\pi<\phi+\lambda\theta<2\pi$ to its image θ'. The branch index is the local torsion of the period-one orbit in the flow for which R^1 is the return map. As ϕ increases, the flow is directed toward branches with successively larger local torsion.

The return map R^1 has two important symmetries.

1. Translation invariance. The map R^1 is invariant under translation $\phi \to \phi + 2\pi$

$$\theta' = \pi/2[1-\cos(\phi+2\pi+\lambda\theta)] = \pi/2[1-\cos(\phi+\lambda\theta)] \ . \tag{5.5}$$

Under translation, all branch indices are increased by 2. This simply reflects the fact that the free rotation involves one more rotation about the bottom of the well for period $T+\tau$ than for period T. The periodicity in ϕ reflects the superstructure in the bifurcation diagram of the generic nonlinear oscillator. Each island in the superstructure is labeled by an integer i, which is half the branch index of the return map. This invariance is responsible for the symmetries (Sec. IV B) of direct horseshoe to direct horseshoe and reverse horseshoe to reverse horseshoe.

2. Rotation invariance. The map R^1 is invariant under rotation about the center of any branch. The θ' coordinate of the center of a branch is $\pi/2$. The θ coordinate at the center of branch N must obey $\cos(\phi+\lambda\theta_c)=0$. Under these conditions

$$\begin{aligned} &\theta' = \pi/2 + \Delta\theta' = \pi/2[1-\cos(\phi+\lambda\theta_c+\lambda\Delta\theta)] \ , \\ &\Delta\theta' = (-1)^N \pi/2 \sin(\lambda\Delta\theta) \ . \end{aligned} \tag{5.6}$$

The rotation invariance is

$$(\Delta\theta, \Delta\theta') \to (-\Delta\theta, -\Delta\theta') \ . \tag{5.7}$$

Under this invariance, the branch indices map to $N \to N$, $N+1 \to N-1$, and more generally $N+k \to N-k$.

There is a related symmetry that is useful if we plot fixed points of this map (or any of its iterates) as a function of ϕ. By fixing $\theta'=\theta$ and writing $\phi=\phi_c+\Delta\phi$, we find, following the arguments above,

$$\Delta\theta' = (-1)^N \pi/2 \sin(\Delta\phi) \ , \tag{5.8}$$

so the related rotation symmetry is

$$(\Delta\phi, \Delta\theta') \to (-\Delta\phi, -\Delta\theta') \ . \tag{5.9}$$

These rotation symmetries map direct horseshoes to reverse horseshoes and are responsible for the symmetries described in Sec. IV B.

D. Construction of R^2 from R^1

Figure 10 shows R^1 and R^2 for $\lambda=1.8$ and $\phi=0.1+0.1\times 2\pi$. The map R^1 has an interior maximum and minimum at M and m and boundary maxima and minima on the left and right boundaries ($\theta=0,\pi$) at L and R. These maxima and minima define the locations of all critical points of R^2.

For the parameter values used, R^1 has three branches in the interval $0 \le \theta \le \pi$ labeled 0, 1, and 2. Therefore R^2 can have at most nine branches labeled 00,01,02,12,11,10,20,21,22 in this interval (cf. Fig. 6).

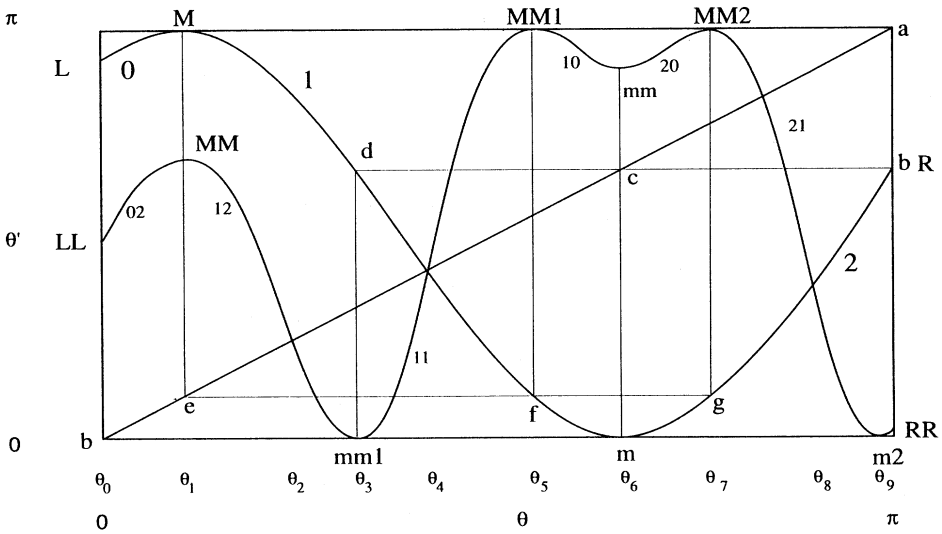

FIG. 10. The return map $\theta' = R^1(\theta) = (\pi/2)[1 - \cos(\phi + \lambda\theta)]$ and $R^2 = R^1 \circ R^1$ for $\lambda = 1.8$ and $\phi = 0.1 + 0.1 \times 2\pi$. The map R^2 can be constructed from R^1 by following the procedure outlined in the text. The fixed point on branch 11 identifies a symmetric period-one orbit of the Duffing oscillator while the fixed points on branches 12 and 21 identify a pair of asymmetric period-one orbits.

Branches 0* of R^2 occur to the left of M (at θ_1); branches 1* occur between M and m at θ_1 and θ_6; branches 2* occur to the right of m at θ_6. Distinct branches of R^2 are separated by critical points. Therefore, by continuity the branches of R^2 for the parameters used are 02,12,11,10,20,21.

The critical points of R^2 are determined from the boundary and interior maxima and minima of R^1 as follows. The critical point M on R^1 separating branches 0 and 1 is the first iterate of θ_1 and the critical point MM on R^2 separating branches 0* from 1* is the second iterate of θ_1. This can be found by the usual construction following the diagonal (path $M\,a\,R\,MM$). In the same way the minimum m at θ_6 separates branches 1 and 2 on R^1 and the second iterate at mm (follow path $m\,b\,L\,mm$) separates branches 1* and 2* on R^2. Three branches 12, 11, and 10 of R^2 exist between MM and mm. They are separated by the critical points $mm1$ and $MM1$. The critical points at $\theta' = 0, \pi$ are the inverse images of m and M, respectively. That is, $mm1$ is located by following the path ($m\,c\,d\,mm1$) and $MM1$ is obtained by following path ($M\,e\,f\,MM1$). This construction also produces $MM2$ ($M\,e\,g\,MM2$), which separates branches 20 and 21. The values LL and RR are second iterates of $\theta = 0$ and π.

We observe that mm on R^2 over θ_6 is a local minimum because L on R^1 is a boundary minimum. If L were a boundary maximum, mm would be a local maximum. Similarly, MM on R^2 over θ_1 is a local maximum because R on R^1 is a boundary maximum. Finally, we observe that the fixed point at θ_4 on R^1 is also a fixed point for R^2. This lifts to the symmetric period-one orbit (11) in the Duffing system. The two fixed points of R^2 at θ_2 and θ_8 are not fixed points of R^1 and therefore describe a symmetric pair of asymmetric period-one orbits (12) and (21) in the Duffing system.

VI. MORPHOLOGY OF MAPS

A periodic orbit of either a nonlinear oscillator or the Duffing oscillator with symbol sequence $(a_1 a_2 \ldots a_p)$, which exists when the drive period is T, is replaced by a corresponding periodic orbit with symbol sequence $(a'_1 a'_2 \ldots a'_p)$ when the drive period is $T + \tau$. Here $a'_j = a_j + 2$. For this to occur, periodic orbits must be created and annihilated as T is increased. This creation and annihilation process is systematic and is in turn determined by the systematic creation and annihilation of branches in the return maps R^1 and R^2. The branches are created and annihilated in boundary catastrophes [29,30].

A. Creation and annihilation of branches in R^1

We illustrate the morphology of R^1 by fixing $\lambda = 1.8$ and increasing ϕ by 2π. The maps R^1 and R^2 are shown in Fig. 10 for $\phi = 0.1 + 0.1 \times 2\pi$. For this value of ϕ the return map R^1 has only three branches labeled 0, 1, and 2 in the interval $0 \le \theta \le \pi$. The return map R^2 has seven branches (02,12,11,10,20,21,22) in this interval. As ϕ is increased, the map R^1 moves rigidly to the left. Branch 0 disappears in a boundary catastrophe as the maximum M moves to the left of $\theta = 0$ and branch 1 begins to decrease in measure. While this occurs at the left-hand boundary $\theta = 0$, branch 2 increases in measure until it completely spans the range from $\theta' = 0$ to π when a maximum of R^1 reaches $\theta = \pi$. Thereafter, branch 3 (which is to the right of the interval $\theta \in [0, \pi]$ for $\phi = 0.1 + 0.1 \times 2\pi$ and is therefore not shown in Fig. 10) begins to grow at the right-hand edge $\theta = \pi$, branch 1 continues to shrink at the left-hand edge, and branch 2 remains unchanged in measure until the minimum at θ_6 crosses $\theta = 0$, at which point branch 2 begins to shrink. As ϕ increases, new branches appear at $\theta = \pi$ and grow, while old branches shrink and finally disappear at $\theta = 0$.

We might therefore expect that orbits are created by saddle-node bifurcations near $\theta = \pi$ and are annihilated by inverse saddle-node bifurations near $\theta = 0$. This is the case and can readily be seen for the period-one orbits which exist in each branch. In Fig. 10, as the maximum which separates branches 2 and 3 (to the right of $\theta = \pi$)

approaches $\theta=\pi$, a tangency occurs between the map R^1 and the diagonal $\theta'=\theta$ near $\theta=\pi$. This tangency marks the saddle-node bifurcation of two period-one orbits. As ϕ continues to increase, the two fixed points move apart. One remains on branch 2. The other moves over the maximum separating branches 2 and 3 and then exists on branch 3. This fixed point is a node and may become a flip saddle if it undergoes a period-doubling bifurcation. As ϕ continues to increase, the period-one orbit on branch 3 moves toward the minimum which separates branches 3 and 4. As this minimum approaches $\theta=0$, the fixed point on branch 3 moves through the minimum onto branch 4, where it is annihilated in an inverse saddle-node bifurcation with the fixed point on branch 4. For this value of ϕ all periodic orbits that involve the symbol 3 no longer exist, since branch 3 is no longer present in the return map.

When ϕ has increased by 2π: $\phi=0.1+0.1\times 2\pi+2\pi$, the maps R^1 and R^2 are identical to those shown in Fig. 10, except that all branch labels have increased by 2 ($0\rightarrow 2$, $1\rightarrow 3$, $2\rightarrow 4$). To each periodic orbit which exists for $\phi=0.1+0.1\times 2\pi$ there is a corresponding orbit at $\phi=0.1+1.1\times 2\pi$.

B. Creation and annihilation of branches on R^2

Changes in the number of branches of the return map R^2 are associated with boundary catastrophes, as is the case for R^1. Boundary catastrophes occur when a minimum or maximum of R^1 occurs at $\theta=0$ or π as ϕ increases. The boundary catastrophes associated with a maximum at $\theta=0$ or a minimum at $\theta=\pi$ are similar to each other. The boundary catastrophes associated with a minimum at $\theta=0$ or a maximum at $\theta=\pi$ are also similar.

We illustrate this branch morphology for the map R^2 shown in Fig. 10 and consider the changes which occur as ϕ is increased by 2π. We first consider processes which annihilate branches, that is, which occur at the left-hand boundary $\theta=0$. Then we treat processes which create branches, which occur at $\theta=\pi$.

As ϕ is increased, the map R^1 moves rigidly to the left. As the boundary minimum L approaches M (e.g., $\theta=0$, $\theta'=\pi$) the local minimum at mm approaches $\theta'=\pi$. The three critical points $MM1$, mm, and $MM2$, which bound branches 10 and 20, approach each other. At the boundary catastrophe of the critical point M at $\theta=0$, the critical points $MM1$, mm, and $MM2$ become triply degenerate. As M moves below $\theta=0$, branch 0 ceases to exist for the map R^1 and branches 10 and 20 cease to exist for R^2. The three critical points $MM1$, mm, and $MM2$ are now replaced by a single critical point mm over m (or θ_6). This is a local minimum which separates branches 11 and 21. As ϕ continues to increase, the minimum at mm approaches the minima at $mm1$ and $mm2$. These three critical points separate branches 11 and 21. As the minimum separating branches 1 and 2 of R^1 approaches $\theta=0$, the three critical points $mm1$, mm, and $mm2$ annihilate in a symmetry restricted cusp catastrophe. When m moves below $\theta=0$, branch 1 ceases to exist for the map R^1 and branches 11 and 21 cease to exist for R^2.

Branch creation morphology is similar to branch annihilation morphology. Beginning again with the return map shown in Fig. 10 we consider what happens as ϕ is increased. The maximum R at $\theta=\pi$ approaches $\theta'=\pi$ and branch 22 for R^2 begins to grow. When the maximum separating branches 2 and 3 (to the right of $\theta=\pi$ in Fig. 10) on R^1 occurs at $\theta=\pi$ there is a triply degenerate critical point bounding branch 22 at $\theta=\pi$ for R^2. When this maximum moves below $\theta=\pi$, the triply degenerate critical point on R^2 splits into three isolated critical points. These three critical points and π bound the three new branches 23, 33, and 32. As ϕ continues to increase, the minimum separating 23 and 33 approaches $\theta'=0$. This minimum reaches $\theta'=0$ when the minimum on R^1, which separates branches 3 and 4, occurs at $\theta=\pi$. This initiates another boundary catastrophe. The minimum separating branches 23 and 33 becomes triply degenerate and as the minimum on R^1 separating branches 3 and 4 moves below $\theta=\pi$, the three critical points on R^2 separate, bounding new branches 24 and 34 between branches 23 and 33.

Throughout this process a series of period-one orbits is created and annihilated in a sequence of direct and inverse saddle-node bifurcations. These occur whenever a tangency occurs between R^2 and the diagonal $\theta'=\theta$. Fixed points of R^2 (e.g., ii, $i=1,2,3$), which are also fixed points of R^1 (e.g., i), are symmetric orbits. Others (e.g., ij,ji with $i\neq j$) occur as symmetric pairs of asymmetric period-one orbits. Once again, after ϕ has increased by 2π to $0.1+1.1\times 2\pi$, the return map R^2 is identical to that shown in Fig. 10 for $\phi=0.1+0.1\times 2\pi$, except that all branch labels have increased by 2 (e.g., branch $12\rightarrow$branch 34).

VII. SYSTEMATICS OF ORBIT CREATION AND ANNIHILATION

In the preceding section we investigated the systematics of branch creation and annihilation as a function of increasing control parameter ϕ for the return maps R^1 and R^2. In this section we investigate the systematics of orbit creation and annihilation as ϕ increases. First, we investigate the creation and annihilation of period-one orbits and show how the local torsion of the nodes changes systematically with ϕ. Then we investigate the properties of period-doubling cascades and the mechanisms involved in saddle-node bifurcations of higher-period orbits.

A. Period-one backbone of R^1

In Fig. 11 we plot the fixed point argument $\phi+\lambda\theta$ as a function of ϕ, for the range $0\leq\phi\leq 5\times 2\pi$. The computation is carried out for $\lambda=1.8$. We see that a number of saddle-node bifurcations occur at points of vertical tangency. Branch labels (local torsion) are used to identify each branch. The branch which exists between $\phi+\lambda\theta=n\pi$ and $(n+1)\pi$ has branch label n.

From Fig. 11 we see that direct saddle-node bifurcations occur at values of $(\phi,\phi+\lambda\theta)\sim(\pi,3\pi),(3\pi,5\pi),(5\pi,7\pi),\ldots$. Inverse saddle-node bifurcations occur at $(2\pi,2\pi),(4\pi,4\pi),(6\pi,6\pi),\ldots$.

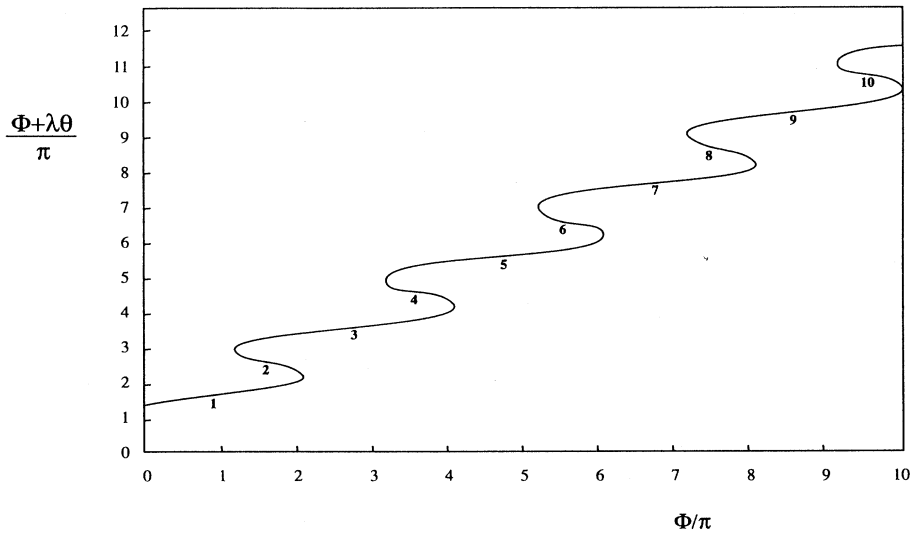

FIG. 11. Period-one snake for the map R^1. Saddle-node bifurcations which occur at $(\phi,\phi+\lambda\theta) \sim [(2n+1-\lambda)\pi, (2n+1)\pi]$ create branches $2n$ and $2n+1$. Inverse saddle-node bifurcations which occur at $\sim(2n\pi,2n\pi)$ annihilate branches $2n$ and $2n-1$.

The bifurcation which occurs at $(\pi,3\pi)$ creates branches 2 and 3. Branch 2 exists between $(\pi,3\pi)$ and $(2\pi,2\pi)$, where it is annihilated in an inverse saddle-node bifurcation with branch 1. Branch 3 exists between $(\pi,3\pi)$ and $(4\pi,4\pi)$, where it is annihilated in an inverse saddle-node bifurcation with branch 4.

Even branches are created as regular saddles and change neither their stability properties nor local torsion while they exist. Odd branches are more interesting. For example, when branch 3 is created in a saddle-node bifurcation with branch 2, the two orbits have local torsion 2. As ϕ increases, the stable node on branch 3 becomes a stable focus and its local torsion smoothly increases from 2 to 3. When the local torsion reaches 3, the node becomes a stable flip (or alternating) node and then a flip saddle as it loses its stability and initiates a period-doubling cascade. As ϕ is further increased, branch 3 approaches branch 4 and an inverse saddle-node bifurcation becomes imminent. The period-doubling cascade reverses itself and the flip saddle becomes a flip node and then a stable focus. The local torsion of this focus increases smoothly from 3 to 4, the focus becomes a stable node, and this node then undergoes an inverse saddle-node bifurcation with the regular saddle on branch 4 whose local torsion is 4.

The curve of period-one fixed points shown in Fig. 11 is called a period-one snake [5,12,46]. This snake shows how the local torsion systematically "winds up" as the control parameter $\phi=2\pi T/\tau$ increases. The snake is responsible for the superstructure in the bifurcation diagrams of the typical nonlinear oscillator and the Duffing oscillator. Bifurcation peninsulas are built on the odd branches of this snake. These branches are bounded by direct and inverse saddle-node bifurcations with the adjacent even branches.

As the Lyapunov exponent λ changes, the shape of the snake changes slightly. Inverse saddle-node bifurcations still occur at $(\phi,\phi+\lambda\theta)\sim(2\pi n,2\pi n)$. Branches $2n-1$ and $2n$ are annihilated at these points. Direct saddle-node bifurcations occur at $\sim((2n+1-\lambda)\pi,(2n+1)\pi)$. Branches $2n$ and $2n+1$ are created at these points.

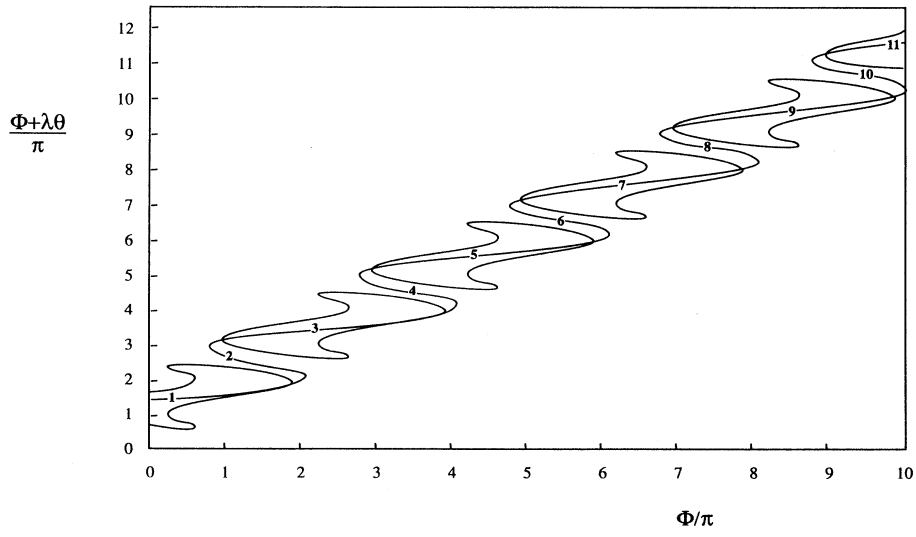

FIG. 12. Fixed points of R^2 describe period-one orbits (the snake) and period-two orbits of R^1. Equivalently, they describe period-one orbits of R^2 which are symmetric (snake) and which form an asymmetric pair (the rest).

B. Period-doubling cascade

Figure 12 shows the fixed points of the map R^2. The orbits defined by these fixed points can be regarded either as period-one (the snake) and period-two (the rest) orbits of R^1 or the symmetric and asymmetric period-one orbits of R^2. The branches identifying these additional fixed points exist only on the odd branches of the period-one snake and have a peculiar shape.

In Fig. 13 we show the period-one orbits and the period-two orbits of R^1 surrounding branch 3. We plot the fixed points $\theta'=\theta$ of R^2 over a range of ϕ extending 4π. In addition, we do not show the period-two orbits along branches 1 and 5 in order to reduce visual clutter. The symbolic dynamics is shown for all branches.

After the period-one orbit on branch 3 is created, it undergoes a period-doubling bifurcation, becoming unstable and creating the orbit 23, which is initially stable. This becomes unstable in a period-doubling bifurcation, not shown. As ϕ increases, branch 2 is annihilated (with 1) and subsequently branch 4 is created (with 5). We might therefore expect that some mechanism exists to replace the symbol 2 in periodic orbits in the cascade with the symbol 4 as ϕ is increased. The mechanism is shown for the period-two orbit; it is the same for all higher-period orbits. A saddle-node bifurcation creates the period-two orbit pair 24 and 34. The three period-two orbits 23, 24, and 34 coexist for some range of ϕ and then the orbit pair 23 and 24 undergoes an inverse saddle-node bifurcation, leaving only the orbit 34 to undergo an inverse period-doubling bifurcation with the period-one orbit 3 before orbits 3 and 4 undergo their inverse saddle-node bifurcation. We note that only three period-two orbits based on the symbols 2, 3, and 4 can be constructed, all coexist for some range of values of ϕ, and the saddle 24 undergoes saddle-node bifurcations with nodes 23 and 34 as a mechanism for exchanging orbit symbolics as the local torsion increases and branch 2 is annihilated and branch 4 is created.

C. Saddle-node bifurcations

We describe here saddle-node bifurcations on branch 3 which create period-three orbits. All other saddle-node bifurcations follow the same pattern, but their fixed point diagrams are much more congested. The fixed point diagram of R^3 is shown in Fig. 14. Once again, we have plotted branches over a range of ϕ of 4π and suppressed period-three orbits built on branches 1 and 5.

In this bifurcation peninsula, the period-one orbits are first created. Subsequently, a saddle-node bifurcation occurs creating a pair of period-three orbits. The symbolic dynamics of these orbits is $M32$, $M=(2,3)$, so that orbits 232 (node) and 332 (saddle) are created. The identification of each branch in Fig. 14 is accomplished as follows. The branch containing the node has a tangency with $\theta'=\pi$ (also $\theta'=0$), for reasons outlined above for the period-one orbits. When we plot the return map $\theta'=R^3(\theta)$, the intersections of this function with the diagonal $\theta'=\theta$ alternately have slope less than one (node)

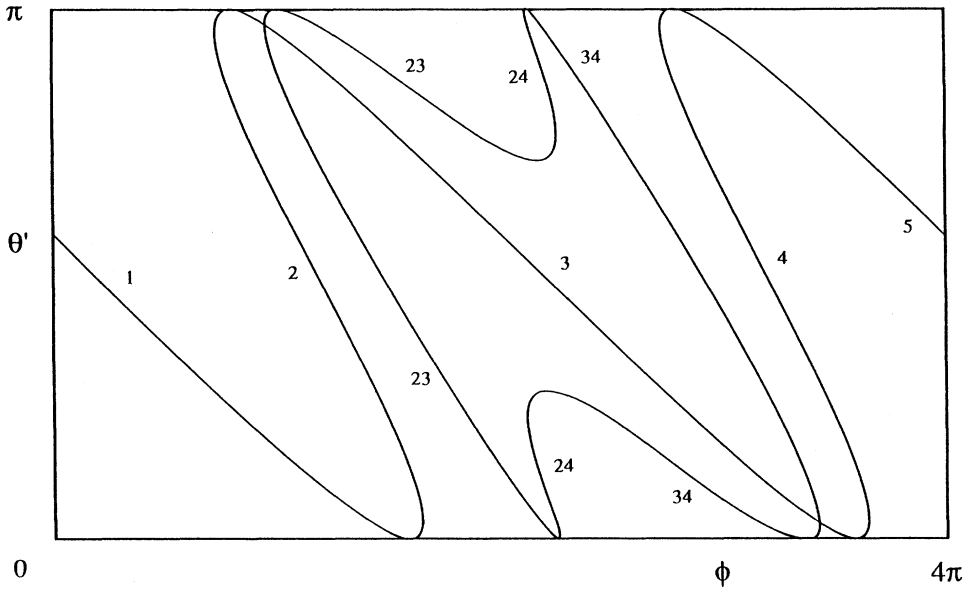

FIG. 13. The fixed points of $\theta'=R^2(\theta)$ are shown in the range $0\leq\phi\leq4\pi$. Period-two orbits on the branches 1 and 5 are not shown. As ϕ is increased, a snake creates the orbit pair (2,3). The saddle 2 annihilates the node 1. The orbit 3 moves over the maximum of the return map, producing the tangency at $\theta'=\pi$, then undergoes a period-doubling bifurcation, creating the period-two orbit 23. This orbit undergoes a period-doubling bifurcation (not shown). A saddle-node bifurcation creates the orbit pair (24,34). The node 34 may initiate a period-doubling cascade. The saddle 24 then undergoes an inverse saddle-node bifurcation with the orbit 23, leaving 34 as the only period-two orbit. The orbit 34 is then "absorbed" by the orbit 3 in an inverse period-doubling bifurcation and then the node 3 and saddle 4 are annihilated in an inverse saddle-node bifurcation. Before the period-two orbits 23 and 34 undergo inverse period-doubling bifurcations, the cascades built on them must first reverse themselves.

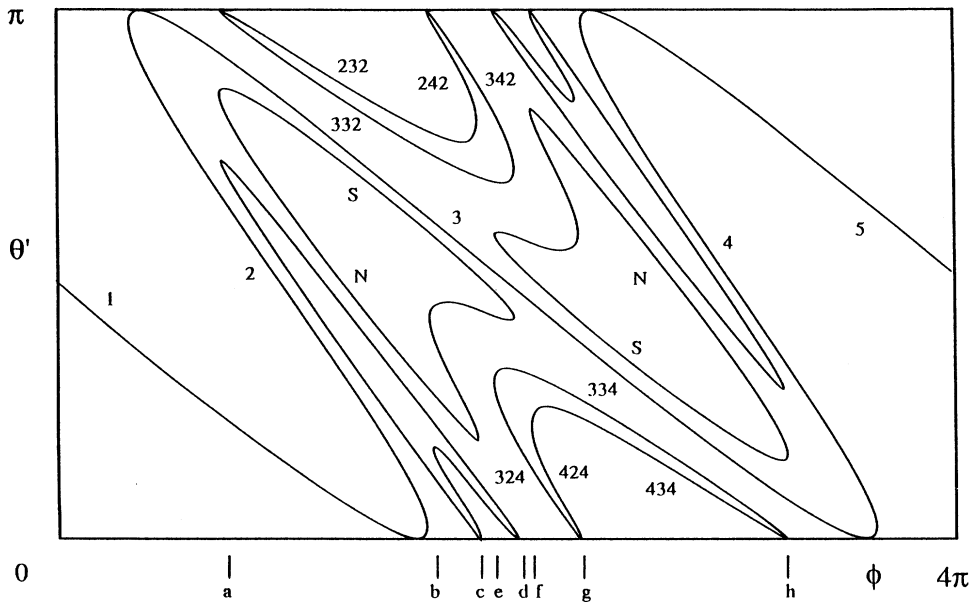

FIG. 14. Fixed points of the return map $\theta'=R^3(\theta)$ are shown for $\lambda=2.2$ in the range $0\leq\phi\leq4\pi$. The period-one snake is shown and all branches (1–5) on it are labeled. Orbits based on the branches 1 and 5 have been suppressed. A saddle-node bifurcation at $\phi=a$ creates the orbit pair $M32$, where $M=(2,3)$. The branches containing the node are tangent to $\theta'=0,\pi$. The stability properties (saddle or node) alternate, because of the geometry of the return map. A second saddle-node bifurcation at b creates the orbit pair $M42$. This is followed by two inverse saddle-node bifurcations at c between $2m2$ and then at d between $3m2$, which annihilate these four orbits, where $m=(3,4)$. A second pair of direct and inverse saddle-node bifurcations creates (at e,f) and annihilates (at g,h) orbits $mM4$. The eight period-three branches are labeled and related to each other by rotation symmetry.

and greater than one (saddle). This observation is sufficient to identify all branches in Fig. 14 as saddle or node branches.

A second saddle-node bifurcation occurs which creates period-three orbits $M42=242$ (saddle) and 342 (node). The node 232 from the first bifurcation and saddle 242 from the second then undergo an inverse saddle-node bifurcation. Then the saddle 332 from the first bifurcation and the node 342 from the second undergo a second inverse saddle-node bifurcation.

For higher-period orbits, a first saddle-node bifurcation creates orbits $M3^*$ and a second creates orbits $M4^*$. The first node and second saddle undergo a first inverse saddle-node bifurcation and subsequently the first saddle and second node undergo the second inverse saddle-node bifurcation, as shown by the following table.

		Inverse saddle-node bifurcation	
		First	Second
direct saddle node bifurcation	First	node	saddle
	Second	saddle	node

(7.1)

The rotation symmetry of R^1 has been used to identify the symbolic dynamics of the remaining four period-three branches. All branches are labeled in Fig. 14. Eight period-three orbits based on the three symbols 2, 3, and 4 exist and all are present on branch 3.

D. How far does the bifurcation sequence go?

After branches 2 and 3 are created in a direct saddle-node bifurcation, periodic orbits on the direct horseshoe (branches 2 and 3) are created in the same order as for the logistic and other unimodal maps [47]. We neglect here those saddle-node bifurcations (e.g., $M42$) which involve branches other than 2 and 3. We now ask how far into the bifurcation sequence we proceed before the bifurcation sequence is reversed.

Roughly speaking, we expect the termination of the bifurcation sequence to be associated with the annihilation of branch 2 in an inverse saddle-node bifurcation. We therefore consider the nongeneric return map R^1 for $\phi=0.80\times2\pi$ and $\lambda=1.83$. This map is nongeneric due to a threefold degeneracy. The two period-one orbits 1 and 2 are doubly degenerate ($\theta_1=\theta_2$) at the tangency that marks their annihilation in an inverse saddle-node bifurcation (local bifurcation) and they are degenerate with the value of R^1 at the boundary $[R^1(\theta=\pi)=R=\theta_1=\theta_2]$. In this nongeneric case all possible orbits on the direct (2 and 3) horseshoe are present.

If λ is smaller than 1.83, then $R>\theta_1=\theta_2$ at the

saddle-node bifurcation. The bifurcation sequence on the (2,3) horseshoe does not go to completion. The last orbit created follows the itinerary beginning with the maximum which separates branches 2 and 3. Immediately after the inverse saddle-node bifurcation, the reversal of period-doubling and saddle-node bifurcations begins.

If λ is larger than 1.83, then $R<\theta_1=\theta_2$ at the saddle-node bifurcation. In this case the bifurcation also fails to go to completion. When orbits are created in saddle-node bifurcations, the first two steps in their itinerary are the maximum separating 2 and 3 and the boundary value at R. As long as $R>\theta_2$ (fixed point of period-one saddle orbit 2) as the inverse saddle-node bifurcation is approached, all orbits remain bounded in the interval $\theta_2<\theta\leq\pi$. However, as soon as $R<\theta_2$ the itinerary enters the domain $\theta<\theta_2$, is confined to the interval $0\leq\theta<\theta_2$, and is attracted to the period-one orbit 1, which is stable for λ slightly larger than 1.83. The boundary crisis terminates the unimodal sequence of bifurcations in the interval $\theta_2<\theta<\pi$ and creates a large window on the period-one orbit in the complementary interval $0<\theta<\theta_2$.

VIII. SYSTEMATICS OF LOCAL TORSION

Within any bifurcation peninsula the local torsion of the stable periodic orbits in the windows evolves in a systematic way with increasing ϕ. The evolution of the local torsion is shown in Fig. 15 for the generic nonlinear oscillator. We show the nongeneric case in which the bifurcation sequence goes to completion. The organization has six parts:

$$I\ \ A\ \ A^R\ \ A^C\ \ A^{RC}\ \ I^{RC}. \tag{8.1}$$

The sequence of local torsions described in (8.1) is described along branch 1 of the generic nonlinear oscillator. Extensions to other branches of this oscillator are straightforward by previously given symmetries.

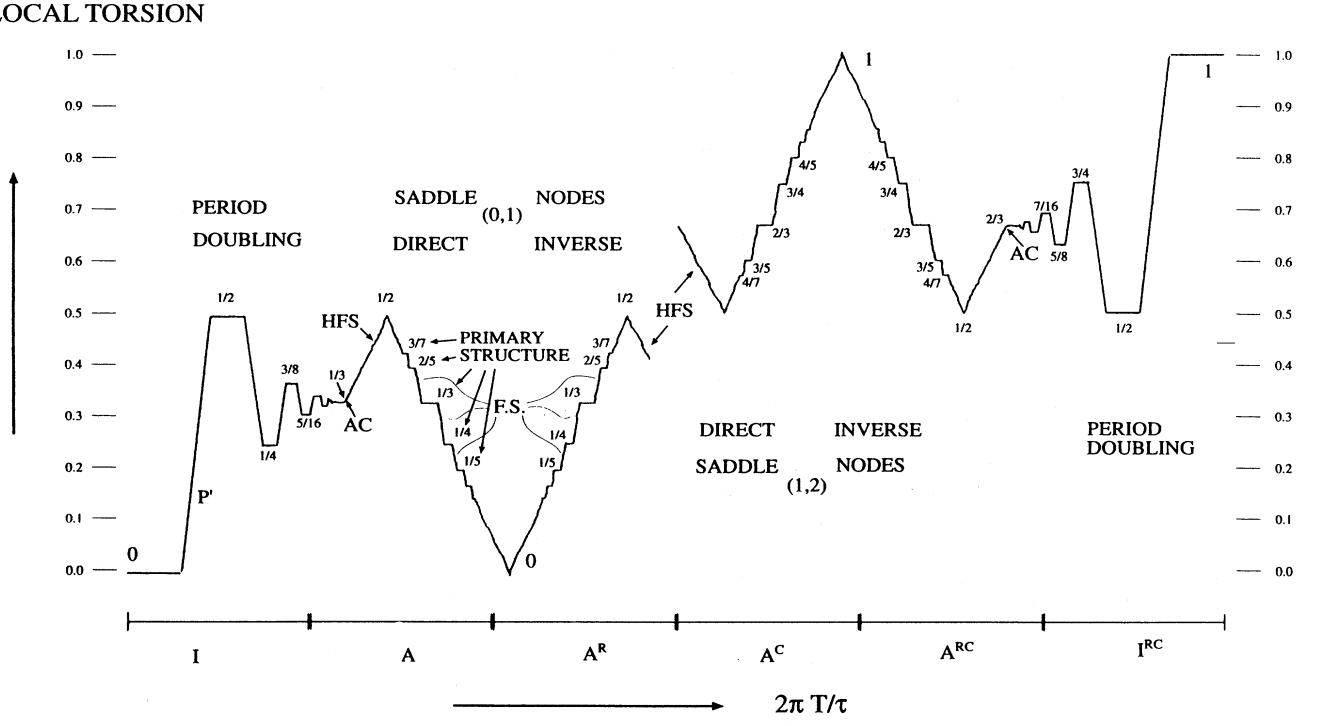

FIG. 15. Behavior of the local torsion on traversing branch 1 of the superstructure of a typical nonlinear oscillator. We show the nongeneric case in which the unimodal bifurcation sequence goes exactly to completion. The local torsion is easily visualized as consisting of six parts. The introduction (I) and conclusion (I^{RC}) describe the period-doubling sequence on the direct (0,1) and inverse (1,2) horseshoes. The local torsion is given by (4.5). The sequence A is the set of local torsions associated with windows created by saddle-node bifurcations in the unimodal sequence (and their associated period-doubling cascades). The local torsion rises from 1/3, the value at the accumulation point of the period-doubling cascade, to 1/2, the value signaling the beginning of the primary series of windows. The largest windows, of the primary series, have local torsions which descend from 1/2 through $p/(2p+1)$ to 1/3, the value of the largest window, and then through values of $1/n$ to 0 as the first and second halves of the primary series are traversed. Interspersed among the primary windows are narrower windows due to the fine structure of well-ordered orbits and extremely narrow windows associated with non-well-ordered orbits. This bifurcation sequence reverses itself, with orbits created last annihilated first. The local torsion sequence is reversed A^R. This direct and reverse bifurcation series is repeated on the reverse horseshoe (1,2), leading to the local torsion sequence A^C, A^{RC}. This nongeneric structure is masked by saddle-node bifurcations, which occur to exchange orbit symbols, and by a large period-one window if the bifurcation sequence goes beyond completion. For the Duffing oscillator the same relation between the local torsion and ϕ is valid, except that the local torsion ranges from 1 to 3.

I. After the saddle 0 and node 1 are created, a period-doubling cascade occurs on branch 1. The sequence of local torsions in this cascade is given by (4.5). The local torsion accumulates at 1/3.

A. This is the sequence of local torsions associated with creation of periodic orbits in unimodal maps. As ϕ increases beyond the accumulation point, a sequence of non-well-ordered orbits is created whose local torsion increases from 1/3 to 1/2. At this point orbits in the primary series of the form 01^{2p} with local torsion $p/(2p+1)$ are created. The local torsion descends from 1/2, the accumulation value of the first half of the primary series as $p \to \infty$, to 1/3, the local torsion of the period-three orbit 001. Beyond the period-three window, which is the largest in the primary series, there is a series of windows of decreasing width associated with Newhouse orbits $0^{n-1}1$ with local torsion $1/n$. These accumulate to local torsion 0 as $n \to \infty$.

Interspersed among the primary windows of the primary structure there are narrower windows associated with the fine structure of well-ordered orbits and very narrow windows associated with the hyperfine structure of non-well-ordered windows. We further note that the local torsion within each window changes systematically as given in (4.5), due to the period-doubling cascade based on each node.

A^R. In the nongeneric case described in Sec. VII D, immediately following the accumulation of the local torsion to 0, periodic orbits are annihilated by inverse saddle-node and period-doubling bifurcations. The periodic orbits are annihilated in the reverse order of their creation. In this region of orbit annihilation the plot of local torsion as a function of ϕ is the mirror (reflected) image of the plot (A) in the previous region.

I^{RC}, A^{RC}, and A^C. On entering a bifurcation peninsula from the other side, that is, by decreasing the value of ϕ, one undergoes the same sequence of bifurcations as encountered by increasing ϕ. The principal difference is that the bifurcation sequences take place on the reverse (1,2) horseshoe rather than on the direct (0,1) horseshoe. Thus the local torsions are complements ($\mathcal{R} \to 1-\mathcal{R}$) of those encountered in the first sequence of bifurcations and the local torsions in the second half of the bifurcation peninsula occur in reverse order to those in the first half. The saddle-node bifurcations that occur to exchange symbols ($0 \to 2$) mask the discontinuity in the local torsion ($1/3 \to 2/3$) between A^R and A^C.

The basic behavior of the local torsion in each bifurcation peninsula outlined in (8.1) is an idealization which is nongeneric. For a typical oscillator the actual bifurcation diagram is a variation on this theme. If the bifurcation does not go to completion ($\lambda < 1.83$), the fold between A and A^R will not occur at $LT=0$. In the complementary case that $\lambda > 1.83$, a wide period-one window will appear between A and A^R and these two sequences will not be mirror images of each other. In addition to this, the return map has coexisting basins of attraction, some belonging to the saddle-node pairs created as a mechanism for transferring symbols from one bounding branch (0) to another (2). These nodes may serve to mask some of the regularities displayed in Fig. 15, including that between A^R and A^C.

The relation between the local torsion and ϕ for the Duffing oscillator is also given in Fig. 15 (which has been constructed for nonlinear oscillators). The only difference between the two cases is in the vertical scale. For the nonlinear oscillator the local torsion ranges from 0 to 1 on the direct and inverse horseshoe (zero torsion lift). For the Duffing oscillator on the iterates of these branches the local torsion ranges from 1 to 3 [cf. Eqs. (4.9) and (4.10)].

IX. SUMMARY

Nonlinear oscillators have been studied extensively in the past. The bifurcation diagrams of these oscillators exhibit similarities and regularities over a broad range of control parameter values. In the control parameter plane [driving amplitude, driving frequency or (λ, T)] there are "resonance horns" or bifurcation peninsulas. These are regions in the control parameter space in which many bifurcations occur (Fig. 1). These regions in control parameter space are separated from each other (for sufficiently small λ) by arid oceans which contain only period-one orbits. The bifurcation peninsulas are labeled by an integer N, which changes by ± 1 (± 2 for the Duffing oscillator) between adjacent peninsulas. This integer is a topological index: it is essentially the relative rotation rate of the period-one orbit on which the bifurcation peninsula is built.

The objective of this work has been to determine why the regularities in the bifurcation spectrum for a nonlinear oscillator exist and why the bifurcation spectra of many different oscillators exhibit such striking similarities. We have identified the principal features of the bifurcation diagrams with topological indices: global torsion and relative rotation rates. These indices are robust under perturbation and can be identified in bifurcation diagrams of a broad range of nonlinear oscillators. We have determined the systematic behavior of these topological indices and related these indices to the local torsion of periodic orbits. We have developed methods for predicting and verifying the symbolic dynamics of these periodic orbits. In addition, we have determined the mechanisms responsible for periodic orbit creation and annihilation as the control parameter values (principally T) are varied.

The tools we have used in this effort include numerical simulations of the Duffing equation and construction of one- and two-dimensional return maps. We have also relied on topological tools, including the computation of relative rotation rates and the construction of templates. Though a template is a caricature of the flow on a strange attractor, it accurately reflects the topological organization of all periodic orbits embedded in the strange attractor.

Through the use of one- and two-dimensional return maps we have determined how the flow is "pushed" over the template as the control parameter T is varied. This in turn has allowed us to predict the order in which orbits are created and annihilated as a resonance horn is

traversed. The variation in the local torsion of the stable periodic orbit responsible for the windows in each bifurcation region is complicated and summarized in Fig. 15. This figure applies to the typical nonlinear oscillator operating at nongeneric control parameter values. Modifications in this diagram caused by the bifurcation sequence either not going to completion, or proceeding beyond completion, have been described.

The variation of the local torsion with the period of the external drive exhibited by the Duffing oscillator is similar to that shown in Fig. 15 for the generic nonlinear oscillator. The only difference is that the local torsion for the Duffing oscillator (on branches 0, 1, and 2) extends from 1 to 3, whereas that for other nonlinear oscillators (on the same branches) extends from 0 to 1. This is simply a reflection of the fact that in the Duffing oscillator the rotation occurs in two wells alternatively and there is half a rotation in moving from well to well.

[1] G. Duffing, *Erzwungene Schwingungen bei Veränderlicher Eigenfrequenz und ihre Technische Bedeutung* (Vieweg, Braunschweig, 1918).
[2] W. S. Loud, Duke Math. J. **24**, 63 (1957).
[3] Y. Ueda, J. Stat. Phys. **20**, 181 (1979); Int. J. Bif. Chaos **1**, 199 (1991).
[4] P. Holmes, Philos. Trans. R. Soc. London Ser. A **292**, 419 (1979).
[5] J. G. Byatt Smith, SIAM J. Appl. Math. **47**, 60 (1983).
[6] S. Sato, M. Sano, and Y. Sawada, Phys. Rev. A **28**, 1654 (1983).
[7] H. Kawakami, IEEE Trans. Circuits Syst. **3**, 248 (1984).
[8] F. C. Moon and G.-X. Li, Physica D **17**, 99 (1985).
[9] U. Parlitz and W. Lauterborn, Phys. Lett. **107A**, 351 (1985).
[10] T. Kurz and W. Lauterborn, Phys. Rev. A **37**, 1029 (1988).
[11] W. Lauterborn and R. Steinhoff, J. Opt. Soc. Am. B **5**, 1097 (1988).
[12] H. G. Solari and R. Gilmore, Phys. Rev. A **38**, 1566 (1988).
[13] J. M. T. Thompson, Proc. R. Soc. London Ser. A **421**, 195 (1989).
[14] N. B. Tufillaro, H. G. Solari, and R. Gilmore, Phys. Rev. A **41**, 5717 (1990).
[15] W. Knop and W. Lauterborn, J. Chem. Phys. **93**, 3950 (1990).
[16] U. Parlitz, V. Englisch, C. Scheffczyk, and W. Lauterborn, J. Acoust. Soc. Am. **88**, 1061 (1990).
[17] C. Scheffczyk, U. Parlitz, T. Kurz, W. Knop, and W. Lauterborn, Phys. Rev. A **43**, 6495 (1991).
[18] V. Englisch and W. Lauterborn, Phys. Rev. A **44**, 916 (1991).
[19] J. W. L. McCallum and R. Gilmore, Int. J. Bif. Chaos **3**, 685 (1993).
[20] S. E. Newhouse, Topology **13**, 9 (1974).
[21] J. W. L. McCallum, Ph.D. thesis, Drexel University, 1993.
[22] J. S. Birman and R. F. Williams, Topology **22**, 47 (1983).
[23] G. B. Mindlin, X.-J. Hou, H. G. Solari, R. Gilmore, and N. B. Tufillaro, Phys. Rev. Lett. **64**, 2350 (1990).
[24] G. B. Mindlin, H. G. Solari, M. A. Natiello, X.-J. Hou, and R. Gilmore, J. Nonlinear Sci. **1**, 147 (1991).
[25] G. B. Mindlin and R. Gilmore, Physica D **58**, 229 (1992).
[26] G. Eilenberger and K. Schmidt, J. Phys. A **25**, 6335 (1992).
[27] U. Parlitz, C. Scheffczyk, T. Kurz, and W. Lauterborn, Int. J. Bif. Chaos **1**, 261 (1991).
[28] R. Gilmore, Int. J. Bif. Chaos **3**, 491 (1993).
[29] V. I. Arnol'd, *Catastrophe Theory* (Springer-Verlag, New York, 1986).
[30] R. Gilmore, *Catastrophe Theory for Scientists and Engineers* (Wiley, New York, 1981).
[31] J. W. Swift and K. Wiesenfeld, Phys. Rev. Lett. **52**, 705 (1984).
[32] Y. Ueda, Ann. N.Y. Acad. Sci. **357**, 422 (1981).
[33] H. G. Solari and R. Gilmore, Phys. Rev. A **37**, 3096 (1988).
[34] F. Papoff, E. Arimondo, F. Fioretto, G. B. Mindlin, H. G. Solari, and R. Gilmore, Phys. Rev. Lett. **68**, 1128 (1992).
[35] P. Glorieux and M. Lefranc, Int. J. Bif. Chaos **3**, 643 (1993).
[36] T. Hall, Phys. Rev. Lett. **71**, 581 (1993).
[37] G. B. Mindlin, R. Lopez-Ruiz, H. G. Solari, and R. Gilmore, Phys. Rev. E **48**, 4297 (1993).
[38] U. Parlitz and W. Lauterborn, Z. Naturforsch. A **41**, 605 (1986).
[39] U. Parlitz and W. Lauterborn, Phys. Rev. A **36**, 1428 (1987).
[40] W. Lauterborn and U. Parlitz, J. Acoust. Soc. Am. **84**, 1975 (1988).
[41] T. Uezu and Y. Aizawa, Prog. Theor. Phys. **68**, 1907 (1982).
[42] T. Uezu, Phys. Lett. **93A**, 161 (1983).
[43] P. Beiersdorfer, J. M. Wersinger, and Y. Treve, Phys. Lett. **96A**, 296 (1983).
[44] P. Beiersdorfer, Phys. Lett. **100A**, 379 (1984).
[45] Codes for computing relative rotation rates and linking numbers are available on request.
[46] K. T. Alligood, Trans. Am. Math. Soc. **292**, 713 (1985).
[47] P. Coullet and J. P. Eckmann, *Iterated Maps on the Interval as Dynamical Systems* (Birkhäuser, Boston, 1980).